Astronomy & Astrophysics proofs
July 21, 2022
©ESO 2022

arXiv:1904.01454v1 [astro-ph.HE] 2 Apr 2019

Hard and bright gamma-ray emission at the base of the *Fermi* bubbles

L. Herold [⋆1] and D. Malyshev [⋆⋆1]

Erlangen Centre for Astroparticle Physics, Erwin-Rommel-Str. 1, Erlangen, Germany

July 21, 2022

ABSTRACT

Context. The *Fermi* bubbles (FBs) are large gamma-ray emitting lobes extending up to 55° in latitude above and below the Galactic center (GC). Although the FBs were discovered 8 years ago, their origin and the nature of the gamma-ray emission are still unresolved. Understanding the properties of the FBs near the Galactic plane may provide a clue to their origin. Previous analyses of the gamma-ray emission at the base of the FBs, what remains after subtraction of Galactic foregrounds, have shown an increased intensity compared to the FBs at high latitudes, a hard power-law spectrum without evidence of a cutoff up to approximately 1 TeV, and a displacement of the emission to negative longitudes relative to the GC.

Aims. We analyze 9 years of *Fermi* Large Area Telescope data in order to study in more detail than the previous analyses the gamma-ray emission at the base of the FBs, especially at energies above 10 GeV.

Methods. We use a template analysis method to model the observed gamma-ray data and calculate the residual emission after subtraction of the expected foreground and background emission components. Since there are large uncertainties in the determination of the Galactic gamma-ray emission towards the GC, we use several methods to derive Galactic gamma-ray diffuse emission as well as the contribution from point sources in order to estimate the uncertainties in the emission at the base of the FBs.

Results. We confirm that the gamma-ray emission at the base of the FBs is well described by a simple power law up to 1 TeV energies. The 95% confidence lower limit on the cutoff energy is about 500 GeV. It has larger intensity than the FBs emission at high latitudes and is shifted to the west (negative longitudes) from the GC. If the emission at the base of the FBs is indeed connected to the high-latitude FBs, then the shift of the emission to negative longitudes disfavors models where the FBs are created by the supermassive black hole at the GC. We find that the gamma-ray spectrum can be explained either by gamma rays produced in hadronic interactions or by leptonic inverse Compton scattering. In the hadronic scenario, the emission at the base of the FBs can be explained either by several hundred supernova remnants (SNRs) near the Galactic center or by about 10 SNRs at a distance of ~ 1 kpc. In the leptonic scenario, the necessary number of SNRs that can produce the required density of CR electrons is a factor of a few larger than in the hadronic scenario.

Key words. Gamma rays: general – Galaxy: center – Galaxy: halo – ISM: jets and outflows

Contents

1 Introduction **2**

2 Data selection **4**

3 Modeling of the *Fermi* bubbles at low latitudes **4**

3.1 East-west asymmetry in the data . . 4
3.2 Low-energy data as a background model 4
3.3 Rectangles model of the bubbles . . 6
3.4 GALPROP model of the foreground and PS refitting 7

⋆ e-mail: laura.herold@fau.de
⋆⋆ e-mail: dmitry.malyshev@fau.de

4 Morphology and spectrum of the gamma-ray emission at the base of the FBs **7**
4.1 Latitude and longitude profiles . . . 7
4.2 Comparison of the spectra at different latitudes 9
4.3 Parametric model of the gamma-ray spectrum at low latitudes 9
4.4 IC model of the gamma-ray emission 10
4.5 Hadronic model of gamma-ray emission 12
4.6 Summary of the spectral analysis . . 13

5 Intepretation **13**
5.1 Emission near the GC scenario . . . 13
5.2 A nearby SNR or a superbubble scenario 15

6 Conclusions **18**

A Modeling and systematic uncertainties **21**

B Gamma distribution as a likelihood for smoothed data **21**

C Modeling uncertainty of ISRF near the GC **22**

1. Introduction

The *Fermi* bubbles (FBs) are one of the most spectacular and unexpected discoveries in the *Fermi* Large Area Telescope (LAT) data (Su et al. 2010). The FBs extend up to 55° in latitude above and below the Galactic center (GC), they have a well-defined edge and a relatively uniform intensity across the surface, apart from a "cocoon" in the south eastern part of the bubbles (Su & Finkbeiner 2012; Ackermann et al. 2014). The intensity spectrum is $\sim E^{-2}$ at GeV energies with a cutoff or a softening around 100 GeV at latitudes $|b| > 10°$ (Ackermann et al. 2014). The origin of the FBs is attributed either to an emission from the supermassive black hole (SMBH) at the center of our Galaxy or to a period of starburst activity which resulted in a combined wind from supernova (SN) explosions of massive stars (Su et al. 2010). The gamma-ray signal up to 100 GeV can be produced either by interactions of hadronic cosmic rays (CR) with gas (hadronic model) or by inverse Compton (IC) scattering of high energy electrons and positrons and the interstellar radiation (leptonic model).

Although the FBs were detected about 8 years ago, their origin is still unresolved. Important insights into their origin can be obtained from the study of the morphology and the spectrum of the FBs near the GC. The spectrum of gamma rays can provide information on the composition of the CR that produce the gamma-ray signal (hadronic vs leptonic CR), as well as the age of the CR (through a cooling cutoff in the leptonic scenario or a break due to escape of high energy CR) and the spectrum of the CR at the source. The morphology of the emission can point to the source of the bubbles: either the SMBH Sgr A* or a recent star-forming region. Previous analyses of the FBs at low latitudes indicated higher intensity of emission near the Galactic plane (GP) and a displacement to negative longitudes (Acero et al. 2016; Ackermann et al. 2017; Storm et al. 2017). The spectrum of the FBs for $|b| < 10°$ is consistent with a power-law $\propto E^{-2}$ without a cutoff up to 1 TeV (Ackermann et al. 2017).

The study of the FBs in the GP is complicated due to bright Galactic diffuse emission components. The π^0 component of the gamma-ray emission is well traced by the distribution of gas, but it has large uncertainties towards the GC due to a lack of kinematic information from the motion of the gas in the Galaxy, which is used to reconstruct the gas distribution (the velocity of the gas in the direction of the GC is perpendicular to the line of sight) as well as the uncertainties in the CO emission along the line of sight to the GC (which is used as a tracer of molecular hydrogen) and large dispersion of velocities of some molecular clouds near the GC. There are also large uncertainties in the distribution of the CR sources and the propagation model near the GC, which make it rather difficult to predict a priori the distribution of the propagated CR in the Galaxy. For the IC component of the gamma-ray emission, there is a significant uncertainty in the interstellar radiation field (ISRF) density near the GC (Popescu et al. 2017; Porter et al. 2017; Niederwanger et al. 2019) in addition to the uncertainties in the CR distribution. There should also be undetected point-like and extended sources, which nevertheless contribute to the total flux. Distribution of CR in the Galaxy can be computed with CR propagation tools, such as GALPROP (Strong et al. 2007). The maps of gamma-ray emission from interactions of CR with gas in different Galactocentric rings and from interaction of CR

electrons and positrons with the ISRF can be used as templates for the corresponding components of gamma-ray emission. The agreement of the gamma-ray data with models based on templates derived with the CR propagation tools is rather poor in the GP (e.g., Porter et al. 2017).

In this paper, we analyze the gamma-ray emission at the base of the FBs and estimate the uncertainties related to modeling of the Galactic foreground and background components. We focus on morphology and spectrum of the FBs at energies from 10 GeV to 1 TeV, where the intensity of the gamma-ray emission from the FBs relative to the other Galactic components is higher than at low energies due to softer spectra of the Galactic components. The study of the FBs at high energies will be also important for future searches with neutrino and Cherenkov telescopes.

We use several methods to determine the Galactic foreground/background emission. Unfortunately the notion of the foreground and background emission may not be well defined if we search for an extended gamma-ray emitting source based on the gamma-ray data itself (rather than using the multi-wavelength data, e.g., to trace the distribution of gas). Here and in the following by foreground/background emission we will mean a steady state (or average) diffuse emission of gamma-rays. The steady state distribution of CR is obtained by averaging in time over many sources, it results in the local CR proton spectrum of $\sim E^{-2.7}$ for energies from a few GeV to about a PeV and $\sim E^{-3.3}$ for the local CR electrons from GeV to TeV energies. If the spectrum of the CR at the source is $\sim E^{-2.0-2.2}$, then the softening of the spectrum of CR protons by $\sim E^{-0.3} - E^{-0.6}$ is due to energy-dependent escape from the Galaxy, while the softening for the CR electrons by $\sim E^{-1}$ is due to cooling. A distinguishing property of a source of CR is that the spectrum of CR at or near the source is much harder than the average (propagated) spectrum of CR. Thus, one can look for the presence of a population of freshly accelerated CR by searching for areas of gamma-ray emission with spectrum harder than average. In particular, one can use an "on-off" analysis to subtract the steady state component of the gamma-ray emission. One of the caveats of this analysis is that even the steady state gamma-ray emission in the "on" region can be more intense than the emission in the "off" region, but in this case the difference of the fluxes would have a soft spectrum characteristic of the propagated CR, unless the difference in flux is much smaller than the flux in both "on" and "off" regions: in this case the difference can have a harder spectrum than the two terms. We use the "on-off" technique as a preliminary check in a search for a population of freshly accelerated CR: the hard spectrum of the difference is a necessary condition for the presence of a population of CR with a spectrum harder than the steady state distribution of CR. It is also a sufficient condition for the presence of a population of CR with a hard spectrum, if the difference has intensity comparable to the overall intensity in the "on" and "off" regions.

Consequently, on consideration that there is a tentative asymmetry in diffuse gamma-ray emission near the GC at high energies with a spectrum harder to the west of the GC relative to the emission to the east of the GC, as a first step, we estimate the amount of the asymmetry by taking the difference in the gamma-ray data to the west and to the east of the GC after masking bright point sources. Second, since the spectrum of the FBs at high latitudes as well as the inferred spectrum at low latitudes is harder than the spectra of the other components of diffuse emission, the contribution of the FBs at energies $\lesssim$ 1 GeV is relatively small. We use the data below 1 GeV as a template of the Galactic foreground emission, which we fit to the data at energies above 1 GeV. The residual emission is used to estimate the contribution from the components with spectra harder than the typical spectra of the steady state diffuse gamma-ray components. Finally, we determine a model for the Galactic gamma-ray diffuse emission using templates for the emission components based on GALPROP calculation[1] (Moskalenko & Strong 1998; Strong et al. 2000, 2004; Ptuskin et al. 2006; Strong et al. 2007; Porter et al. 2008; Vladimirov et al. 2011). In this model, we allow many free parameters, such as rescaling of the π^0 and bremsstrahlung emission in Galactocentric rings and refitting of bright point sources near the GC. With the many free parameters, this model absorbs as much of the gamma-ray emission at the base of the FBs as it can. As a result, the residual emission at the base of the FBs in this model is smaller than the residuals in the other models considered in the paper.

The similarity of the energy spectrum below 100 GeV of the hard and bright emission at the base of the FBs and the FBs at high latitudes as well

[1] `http://galprop.stanford.edu`

as the spatial coincidence of the emission with a continuation of the FBs from high latitudes make the physical correspondence of the two objects very plausible. Nevertheless, their alignment along the line of sight can be accidental and the distance to the two objects can be different, i.e., the FBs may be above and below the GC while the hard component may be at a closer distance, e.g., 1 kpc, from us so that the two objects would be physically unrelated. Thus, we will refer to the hard and bright component as "emission at the base of the FBs" to keep both possibilities open: that the emission is the base of the FBs and that the emission is at a different location along the line of sight towards the base of the FBs. We discuss possible origins of the hard component of emission in Section 5. Section 6 contains conclusions.

2. Data selection

We use 9 years of the *Fermi*-LAT Pass 8 Source class events between August 4, 2008 and August 3, 2017 (*Fermi* Mission Elapsed Time 239557418 s – 523411376 s) with energies between 316 MeV = $10^{2.5}$ MeV and 1 TeV separated in 21 logarithmic energy bins (6 bins per decade). The selection of the events is performed with the standard quality cuts (DATA_QUAL>0)&&(LAT_CONFIG==1). In order to avoid contamination from gamma rays produced in interactions of CR in the Earth atmosphere, we select events with zenith angles $\theta < 100°$, which is sufficient for energies above 316 MeV. We calculate the exposure and point-spread function (PSF) using the *Fermi*-LAT Science Tools package version 10-01-01 available from the *Fermi* Science Support Center[2] with the P8R2_SOURCE_V6 instrument response functions. Figure 1 shows the energy flux of the gamma-ray emission integrated in three energy ranges[3]. For all maps shown in this paper, we use Galactic coordinates centered on the GC in Mollweide projection. For spatial binning we use the HEALPix[4] (Górski et al. 2005) scheme with a pixelization of order 7 ($\approx 0.^\circ46$ pixel size).

[2] `http://fermi.gsfc.nasa.gov/ssc/data/analysis/`

[3] The integral of the energy flux intensity between E_0 and E_1 is defined as $I = \int_{E_0}^{E_1} E \frac{dN}{dE} dE$.

[4] `http://sourceforge.net/projects/healpix/`

3. Modeling of the *Fermi* bubbles at low latitudes

3.1. East-west asymmetry in the data

In order to investigate the asymmetry of the emission at the base of the FBs relative to the GC, we compare the *Fermi*-LAT data east and west of the GC. We mask the 200 point sources (PS) in the Third *Fermi*-LAT source catalog (3FGL, Acero et al. 2015) with the largest flux above 1 GeV. Each PS is masked with a circle of radius $\frac{\delta}{\sqrt{2}} + 0.^\circ5$, where $\delta = 0.^\circ46$ is the characteristic size of the pixels so that $\delta/\sqrt{2}$ is half of the pixel diagonal (if it were a square), while $0.^\circ5$ is comparable to the 68% containment radius of the point-spread function above ≈ 2 GeV. Thus the total radius is about $0.^\circ82$. In order to avoid possible bias by masking more pixels on one side of the GC in the Galactic plane, we symmetrize the PS mask relative to the GC, i.e., we set $m_{-b,-\ell} = 0$ if $m_{b,\ell} = 0$ and vice versa. This PS mask is also used in the following sections (apart from Section 3.4). The data are averaged over regions to the east ($0° < \ell < 10°$) and to the west ($-10° < \ell < 0°$) of the GC at different latitudes. The regions have a latitude width of 4°. The fraction of masked pixels is about 50% within $|b| < 2°$, about 10% for $2° < |b| < 6°$, and less than 5% for $|b| > 6°$.

The difference of the averaged intensity of emission west minus east of the GC is shown in Fig. 2. The error bars represent the statistical errors. The emission for latitudes $b \in (-6°, -2°)$ and $b \in (-2°, 2°)$ shows excess emission to the west of the GC, which remains significant at high energies. The Fermi-LAT exposure within $|b| < 10°$ and $|\ell| < 10°$ is rather uniform; the maximal fractional variation of the exposure in this region for $E > 1$ GeV is less than 4%.

3.2. Low-energy data as a background model

In the previous section we have shown that the west-minus-east difference in the *Fermi*-LAT data in the Galactic plane relative to the GC has a hard spectrum $\sim E^{-2}$ up to 1 TeV. One of the simplest ways to separate the soft component of emission from the hard one is to use the low-energy data as a model of the soft component and subtract it from the data at higher energies. Gamma rays produced in interactions of the steady state Galactic population of CR with gas and ISRF, i.e., the π^0,

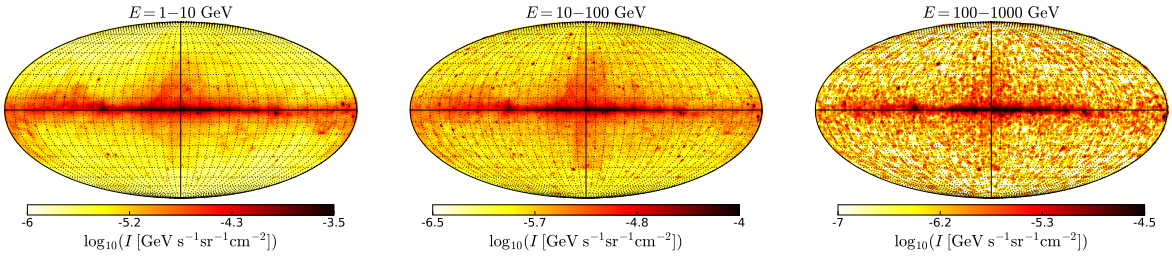


Fig. 1: Energy flux of the *Fermi*-LAT 9 years of Source class data integrated in energy ranges 1 – 10 GeV, 10 – 100 GeV, and 100 GeV – 1 TeV. The maps are represented in logarithmic scale. The map in the energy range 10 – 100 GeV (100 – 1000 GeV) is smoothed with a Gaussian kernel with radius $\sigma = 0.^\circ5$ ($\sigma = 0.^\circ7$). The plots are created with the HEALPix package (Górski et al. 2005) in Mollweide projection with nside = 128 ($\approx 0.^\circ46$ pixel size).

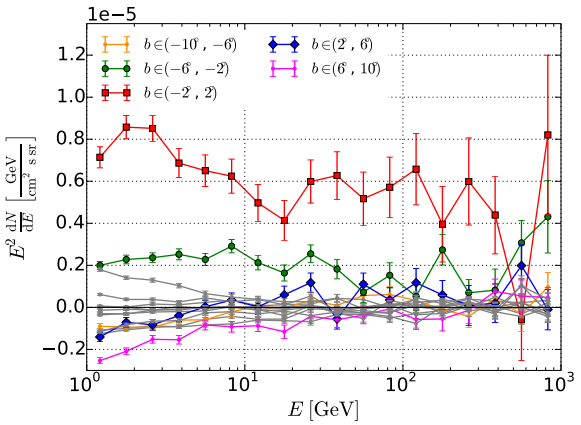


Fig. 2: Difference west minus east in the *Fermi*-LAT intensity relative to the GC after masking bright PSs. The PS mask is symmetrized relative to the GC. The west (east) region is defined between $-10^\circ < \ell < 0^\circ$ ($0^\circ < \ell < 10^\circ$). Grey lines show spectra for latitudes $|b| > 10^\circ$.

bremsstrahlung, and IC components, dominate the gamma-ray emission in the Galactic plane in the energy range $E \lesssim 1\,\mathrm{GeV}$. Consequently, the low-energy *Fermi*-LAT data is a good tracer for the soft components of the diffuse gamma-ray emission in the Galactic plane and can be used to create a spatial template for the Galactic foreground. The 68% containment for the *Fermi*-LAT photons between 316 MeV and 1 GeV (averaged with an E^{-2} spectrum) is about $1.^\circ5$, which is much larger than the sub-degree angular resolution above 1 GeV. In order to compensate for the difference in the angular resolution, we smooth the data in each high-energy bin above 1 GeV with a Gaussian kernel of $\sigma = 1^\circ$ (which corresponds to 68% containment angle of $1.^\circ5$ in 2 dimensions).[5]

We separate the whole sky in latitude stripes of 4° width where the HEALPix pixels are assigned to stripes that contain the centers of the pixels. We parametrize the model in each stripe and each energy bin independently, i.e., in the latitude stripe b for energy bin E and HEALPix pixel with index i the model consists of two terms:

$$M_b(E,i) = k_b(E) \cdot \tilde{N}_b^{\mathrm{low}}(E,i) + c_b(E) \cdot \tau(E,i), \quad (1)$$

where $k_b(E)$ and $c_b(E)$ are coefficients to be determined from the fit to the data. The term $c_b(E) \cdot \tau(E,i)$ is proportional to the exposure $\tau(E,i)$: it accounts for the isotropic extragalactic background and partially compensates for the latitude-dependent IC emission. $k_b(E) \cdot \tilde{N}_b^{\mathrm{low}}(E,i)$ is proportional to the low-energy photon counts summed over $n_{\mathrm{low}} = 3$ energy bins between 316 MeV and 1 GeV rescaled by the ratio of exposures at low and at high energies:

$$\tilde{N}_b^{\mathrm{low}}(E,i) = \frac{1}{n_{\mathrm{low}}} \left(\sum_{\alpha=1}^{n_{\mathrm{low}}} \frac{N(E_\alpha,i)}{\tau(E_\alpha,i)} \right) \tau(E,i), \quad (2)$$

where $N(E_\alpha,i)$ is the number of photons in energy bin E_α and in pixel i.

We determine the parameters $c_b(E)$ and $k_b(E)$ by fitting the model to the *Fermi*-LAT data in energy bins $E > 1\,\mathrm{GeV}$. We maximize the log likelihood of the gamma distribution with respect to parameters $c_b(E)$ and $k_b(E)$ using the Python iminuit optimizer[6]. In order to avoid an overcom-

[5] In general, the width of the Gaussian kernel σ can be obtained by subtracting in quadrature the equivalent widths at low and at high energies $\sigma^2 = \sigma^2_{\mathrm{low}} - \sigma^2_{\mathrm{high}}$. Since $\sigma^2_{\mathrm{low}} \gg \sigma^2_{\mathrm{high}}$, we neglect σ^2_{high} and smooth the data at high energies with $\sigma_{\mathrm{low}} = 1^\circ$.

[6] The gamma distribution $p(x;\tilde{k}+1) = \frac{x^{\tilde{k}}}{\Gamma(\tilde{k}+1)} e^{-x}$ is the probability density function for the parameter x given the observed counts $\tilde{k}$. The counts $\tilde{k}$ are integer for unsmoothed maps and non-integer for the smoothed maps. We discuss the optimization of the model parameters using smoothed maps in Appendix B.

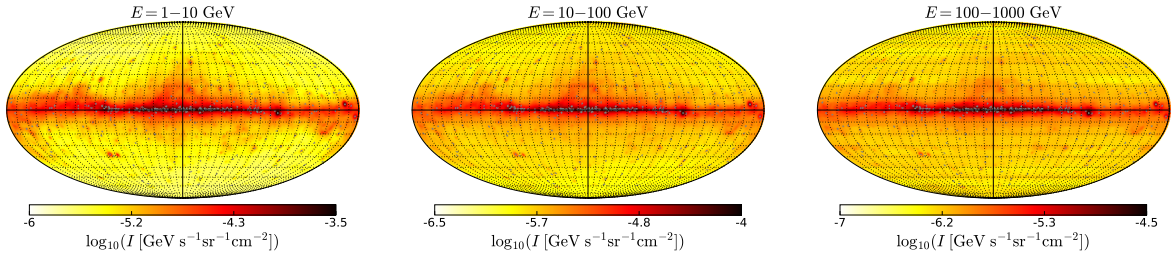


Fig. 3: Energy flux of the diffuse emission model based on the low-energy data (Section 3.2) integrated over three energy ranges.

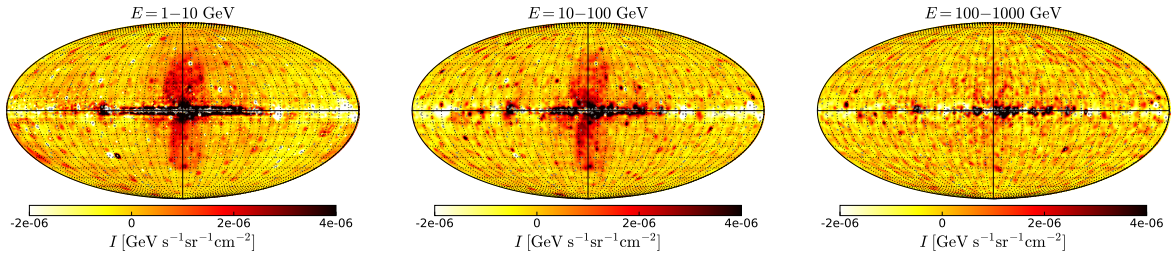


Fig. 4: Energy flux of the residuals of the low-energy model derived in Section 3.2 integrated over three energy ranges.

pensation for the flux from the FBs, the region $-20^\circ < \ell < 20^\circ$ is excluded from the fit, i.e., the fit is performed for the total remaining length of the stripe $20^\circ < \ell < 340^\circ$. In the following, the region $-20^\circ < \ell < 20^\circ$ will be refered to as the FBs region of interest (ROI). Bright PSs are masked with the mask described in Section 3.1.

After we fit the model in each latitude stripe, we interpolate it inside the bubbles ROI. The intensity of the model energy flux integrated in three energy ranges is shown in Figure 3, while the residuals after subtracting the model from the data are presented in Figure 4. The FBs are clearly visible in the first two energy ranges, $E = 1 - 10\,\mathrm{GeV}$ and $E = 10 - 100\,\mathrm{GeV}$. For $E = 100\,\mathrm{GeV} - 1\,\mathrm{TeV}$ the statistics are low, but one can still see an excess near the GP. There are other regions of large residuals in the Galactic plane as well as at high latitudes. These are diffuse and point-like sources with spectra harder than the average spectra of Galactic and extragalactic sources. In particular, there is a residual in diffuse emission along the Galactic plane within $|\ell| \lesssim 60^\circ$ at energies below 100 GeV. This residual can be due to IC emission, which has a harder spectrum than the average spectrum of the π^0 component, or to a harder spectrum of cosmic rays in the inner Galaxy (Gaggero et al. 2015; Acero et al. 2016; Yang et al. 2016), or to a population of hard PSs in the Galactic plane in the inner parts of the Galaxy. At energies above 100 GeV the residuals are resolved into localized sources, some of which are extended. Apart from the Galactic foreground and background components, there are gamma rays emitted by the interactions of CRs with the Sun and its radiation field (Abdo et al. 2011b) and the Moon (Ackermann et al. 2016). The intensities of the emission from the Sun and the Moon are about an order of magnitude less than the intensity of the emission from the FBs. As a result, these components are not visible on the residual maps at energies above 10 GeV.

3.3. Rectangles model of the bubbles

In the previous subsection, we exclude the ROI of the FBs. In this subsection, we perform the fit over the whole sky and model the emission from the FBs using rectangles. In order to explore the east-west asymmetry of the FBs, we introduce two rectangular templates in each latitude stripe b and energy bin E: one east, $\ell \in (0^\circ, 20^\circ)$, and one west, $\ell \in (-20^\circ, 0^\circ)$, of the GC. The width of the rectangles is 4°, i.e., the same as the width of the latitude stripes. We use the same foreground model as in Section 3.2 plus the isotropic template. Overall, the model has four terms in each energy bin:

$$M_b(E,i) = k_b(E) \cdot \tilde{N}_b^{\mathrm{low}}(E,i) + c_b(E) \cdot \tau(E,i) + R_b^{\mathrm{east}}(E) S_b^{\mathrm{east}}(i) + R_b^{\mathrm{west}}(E) S_b^{\mathrm{west}}(i). \quad (3)$$

where the scaling parameters $k_b(E)$ and $c_b(E)$ and the FBs model parameters $R_b^{\rm east}(E)$ and $R_b^{\rm west}(E)$ are determined independently in each 4° latitude stripe and in each energy bin $E > 1$ GeV by fitting the model to the smoothed *Fermi*-LAT data (see Section 3.2 for details on the smoothing of the data). $S_b^{\rm east}(i)$ and $S_b^{\rm west}(i)$ are step function templates, which are equal to 1 in each latitude stripe b for $0^\circ < \ell < 20^\circ$ and $0^\circ > \ell > -20^\circ$ respectively and 0 otherwise. The energy fluxes of the model and the residuals integrated in the range $E = 10 - 100\,{\rm GeV}$ are shown in Fig. 5.

3.4. GALPROP model of the foreground and PS refitting

In this section we fit the gamma-ray data using a model derived with the GALPROP Galactic cosmic-ray propagation code v54.1. The model for the diffuse emission components is the same as the Sample model in Ackermann et al. (2017). In particular, we use the GALPROP code to calculate templates for the Galactic diffuse emission components. We determine 5 templates in each energy bin for gamma rays produced in interactions of hadronic CR with gas and bremsstrahlung emission corresponding to 5 Galactocentric rings: 0 – 1.5 kpc, 1.5 – 3.5 kpc, and 3.5 – 8 kpc; 8 – 10 kpc, and 10 – 50 kpc. We assume propagation halo height of 10 kpc and radius of 20 kpc and spin temperature 150 K. We use 3 inverse Compton templates corresponding to the three ISRF components: cosmic microwave background (CMB), infrared (IR) emission of dust, and starlight (SL). In addition to GALPROP templates, we use a flat template for the *Fermi* bubbles at latitudes $|b| > 10^\circ$ (Ackermann et al. 2014). We model the Loop I feature using a geometric template (e.g., Figure 2 of Ackermann et al. 2014) based on a polarization survey at 1.4 GHz (Wolleben 2007). Templates for the gamma-ray emission from the Sun and the Moon (Orlando & Strong 2008; Abdo et al. 2011b; Johannesson et al. 2013; Ackermann et al. 2016) are obtained with the *Fermi* Science Tools[7]. We also include, as a GC excess template, DM annihilation with a generalized Navarro-Frenk-White (gNFW) profile with index $\gamma = 1.25$ (Goodenough & Hooper 2009; Abazajian et al. 2014; Calore et al. 2015) and scaling radius $r_{\rm s} = 20$ kpc, as well as the isotropic template to model the non-resolved extragalactic sources.

For the PS, we add sources from the 3FGL catalog (Acero et al. 2015) to form a template in each energy bin. We create independent templates for the Large Magellanic cloud and the Cygnus region. The remaining extended sources are also added in a separate template. The spatial templates for the extended sources are provided by the 3FGL catalog. The PS mask in this section is different from the mask that we have used in the previous sections. We mask the 200 sources with largest flux above 1 GeV outside a 10° circle from the GC. Each source is masked with a circle of $\frac{\delta}{\sqrt{2}}+1^\circ$ radius ($\delta = 0.^\circ46$ is the characteristic size of the pixels), which is larger than the radius of $\frac{\delta}{\sqrt{2}}+0.^\circ5$ used in the previous sections. We do not mask PS within 10° from the GC. Instead, we include independent templates for 40 sources with largest flux between 10 and 100 GeV taken from the column "Flux10000_100000" in the 3FGL catalog. Each source is fit in each energy bin independently, i.e., we do not use the spectral information from the 3FGL catalog. In Figure 6 we show the residual emission plus the *Fermi* bubbles model and the gNFW model summed over energies between 10 and 100 GeV. Due to the model having more free parameters in the Galactic plane relative to the models considered in the previous sections, there are fewer positive residuals in the Galactic plane. There are, however, negative residuals in several locations, which indicates errors in the model. In particular, there is a rather significant negative residual to the east of the GC. Nonetheless, the FBs are clearly visible as well as the bright emission at the base of the FBs which also displays a shift to negative longitudes relative to the GC.

4. Morphology and spectrum of the gamma-ray emission at the base of the FBs

4.1. Latitude and longitude profiles

In order to quantitatively estimate the difference in the intensity of the emission of the FBs at high and at low latitudes, as well as the asymmetry of the gamma-ray emission at the base of the FBs, we plot the latitude profiles to the east and to the west of the GC. In Figure 7 we show the profiles of the energy flux between 10 – 100 GeV as a function of the Galactic latitude for different models of Galactic foreground emission. For the low-energy

[7] `http://fermi.gsfc.nasa.gov/ssc/data/analysis/scitools/solar_template.html`

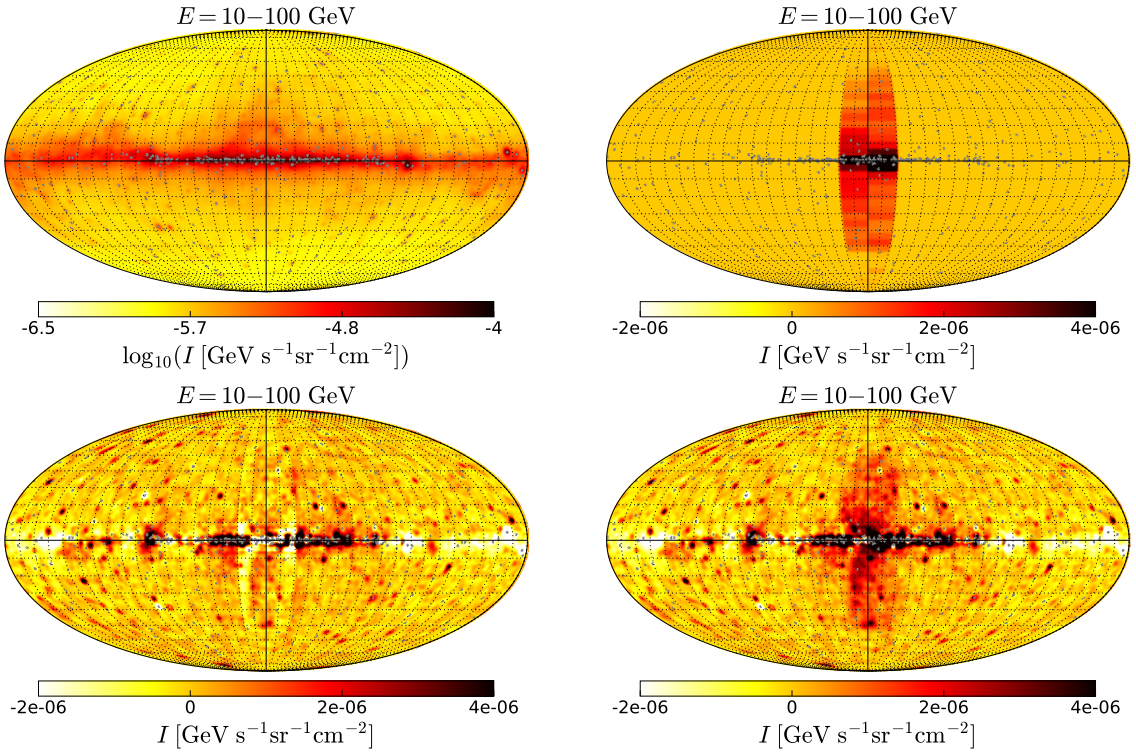


Fig. 5: Energy flux of the diffuse model excluding the rectangles model of the FBs (top left), the rectangles model of the FBs (top right), the residual after subtracting the total model (bottom left), and residuals plus the rectangles model of the FBs (bottom right) derived in Section 3.3 integrated between 10 and 100 GeV.

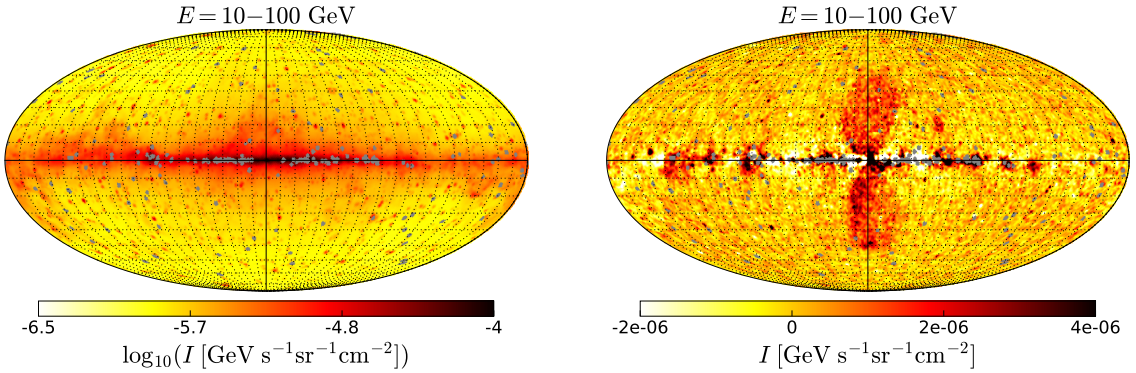


Fig. 6: Energy flux of the background model based on rescaled GALPROP templates (left) and of the residuals plus the FBs and the gNFW component (right) derived in Section 3.4 integrated between 10 and 100 GeV.

model, the profiles show the residual gamma-ray emission, for the rectangles model – the intensity of the rectangles templates model. In case of the GALPROP model, we show the sum of the residual emission, the FBs template, and the GC excess template, as described in Section 3. For comparison we show the latitude profile of the total gamma-ray data (excluding pixels in the PS mask). For positive longitudes, some models overpredict the gamma-ray data near the GP, which leads to negative residuals. For negative longitudes, there is an increase of flux at the base of the FBs by at least a factor of 2 to 6 for all models relative to the gamma-ray emission from the FBs at high latitudes. The results for the GALPROP model differ from the low-energy and rectangles model in the Galactic plane by a factor of 2 to 3. This is due to additional freedom in the GALPROP model related to the usage of several templates in the Galactic plane.

In Figure 8 we show the longitude profiles of the residual flux for the background model based on low-energy data. The excess at $\ell \approx -13^\circ$ for $|b| < 2^\circ$

is probably due to residual emission around the RX J1713 SNR (Abdo et al. 2011a). Consequently, we do not consider it as a part of the emission at the base of the FBs. We associate the excess between $-8^\circ \lesssim \ell \lesssim -2^\circ$ to the base of the FBs. In this paper, we use $\ell \in (0^\circ,\ -10^\circ)$ and $|b| < 6^\circ$ in the calculations of the spectrum of the gamma-ray emission at the base of the FBs.

4.2. Comparison of the spectra at different latitudes

In this section we quantify the hardening of the gamma-ray spectrum at the base of the FBs. We first compare the spectral energy distribution (SED) of the emission at the base of the FBs for different foreground models in Figure 9. The differential flux is averaged over regions to the east, $\ell \in (0^\circ,\ 10^\circ)$, and to the west, $\ell \in (-10^\circ,\ 0^\circ)$, of the GC in a thin stripe covering the Galactic plane $b \in (-2^\circ,\ 2^\circ)$. For comparison, we show the total data (excluding pixels masked by the PS mask) and, on the plot for $\ell \in (-10^\circ,\ 0^\circ)$, the difference in the data west minus east of the GC.

For negative longitudes, all models give similar results. The differential flux of the GALPROP model is smaller than the differential flux of the other models above 10 GeV, which is consistent with the profile plots in Figure 7. The difference of the data west minus east of the GC is similar to the fluxes at the base of the FBs in the low-energy model and in the rectangles model. The spectra at positive longitudes show large oversubtractions and softer spectra.

To compare the behavior of the energy spectra at high energies for different latitudes, we fit a log-parabola plus the fixed foreground model counts to the total smoothed gamma-ray counts in each latitude stripe using the likelihood based on the gamma distribution. We use the following parametrization of the log-parabola function:

$$f(E) = N_0 \left(\frac{E}{1\,\mathrm{GeV}}\right)^{-\alpha-\beta\ln(E/1\,\mathrm{GeV})}. \quad (4)$$

The local "index" of the spectrum at energy E is

$$n \equiv -\frac{\mathrm{d}\ln f}{\mathrm{d}\ln E} = \alpha + 2\beta\ln\left(\frac{E}{1\,\mathrm{GeV}}\right). \quad (5)$$

In Figure 10 we show this log-parabola index n as a function of latitude at $E = 500\,\mathrm{GeV}$. We plot $(2-n)$, which corresponds to the SED index. For positive longitudes, the index is relatively soft ($n > 2$) for most of the latitudes except high latitudes where the gamma-ray statistics are small. For negative longitudes (i.e., West), the index near the GC is significantly harder ($n \approx 2$) than the index at higher latitudes.

4.3. Parametric model of the gamma-ray spectrum at low latitudes

In this section we study the spectrum at the base of the FBs at latitudes $|b| < 6^\circ$. As a baseline model we use the rectangles model of the FBs. We compare a power-law model of the energy spectrum with a power-law and an exponential cutoff model

$$\frac{dN}{dE} = N_0 \left(\frac{E}{1\,\mathrm{GeV}}\right)^{-n} e^{-E/E_{\mathrm{cut}}}. \quad (6)$$

We fit the spectral model added to the fixed background to the total gamma-ray data counts. The best-fit parameters for the rectangles model are reported in Table 1. If the improvement in $2\Delta\log\mathcal{L}$ is less than 1, then we report the power-law model parameters (it turns out that the improvement in $2\Delta\log\mathcal{L}$ is less than 0.1 in the cases when the cutoff is not significant). For the model with a cutoff, we also find the 95% statistical confidence lower limit for the cutoff energy. In the last column we report the minimum among the 95% confidence lower limits for the three models considered in the paper (the low-energy data model, the rectangles model, and the GALPROP templates model). The spectrum of the residuals including the FBs at $\ell \in (-10^\circ,\ 0^\circ)$ is consistent with a power law with an index $2.1-2.2$ up to $E \approx 1$ TeV. The 95% confidence lower limit on the cutoff energy is ~ 500 GeV for latitudes $|b| < 6^\circ$ within $-10^\circ < \ell < 0^\circ$.

As one can see from the spectra in Figure 9, there are large (relative to statistical uncertainty) fluctuations in some of the models. These fluctuations are due to modeling uncertainty of the Galactic diffuse emission. As a result, a fit with a simple function may be sensitive to the starting point (there can be several local minima). In the GALPROP model of the foreground, we also had to constrain the range of the index of the FB's spectrum between 1.5 and 2.5 in the derivation of the 95% confidence lower limit on the cutoff energy.

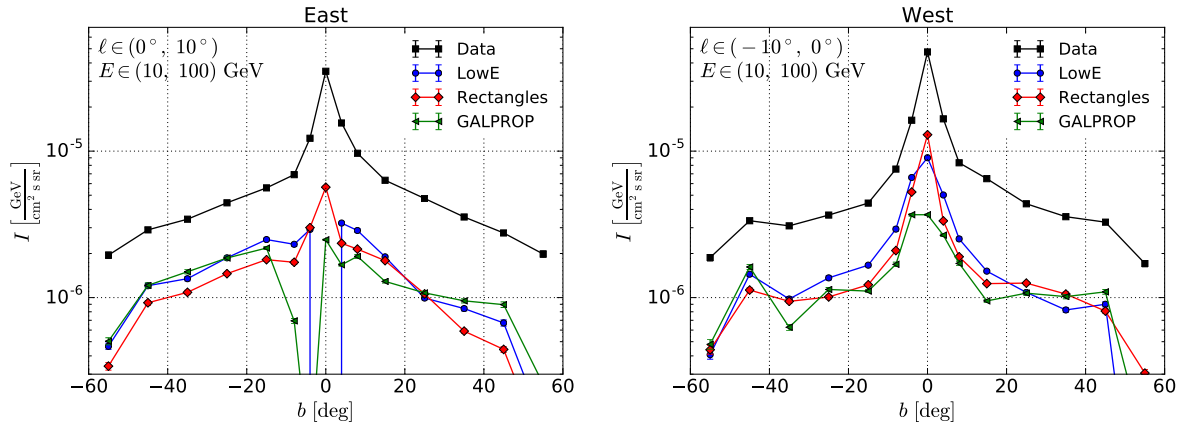


Fig. 7: Latitude profiles of the energy flux between 10 and 100 GeV for the total data excluding the PS mask and for the FBs models for different foreground diffuse emission models to the east and to the west of the GC.

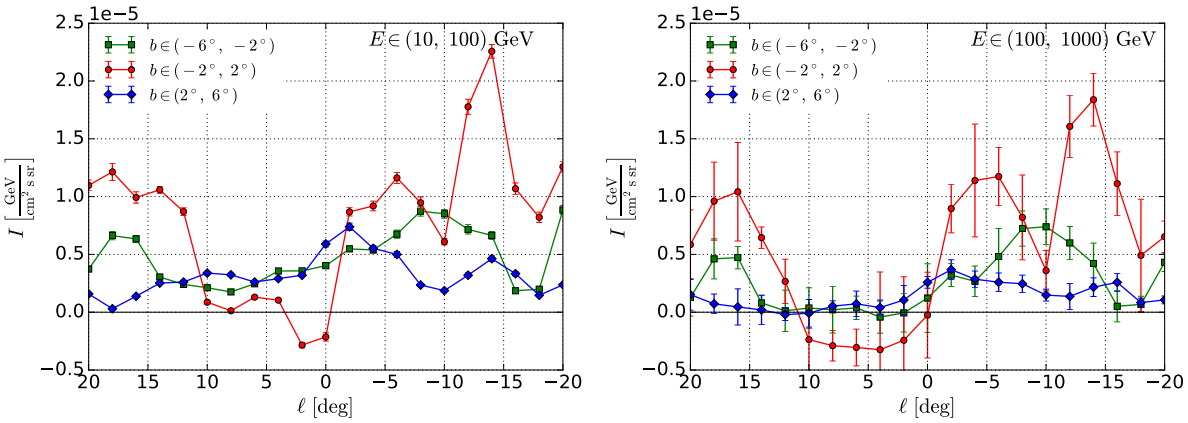


Fig. 8: Longitude profiles of the energy flux between 10 and 100 GeV and between 100 GeV and 1 TeV for the residuals in the low-energy data background model (Section 3.2).

Table 1: Best-fit parameters of the gamma-ray spectrum and the significance of the cutoff for the rectangles model of the FBs. $E_{\rm cut,95\%}$ is the statistical 95% confidence lower limit on the energy cutoff of the FBs spectrum, $E^{\rm min}_{\rm cut,95\%}$ is the minimal 95% statistical lower limit among the models of the FBs in Sections 3.2 – 3.4. There are four cases when the introduction of a cutoff does not lead to improved fit: in all of these cases $2\Delta\log\mathcal{L} < 0.1$ while the formal best-fit values of $E_{\rm cut}$ are larger than 1 TeV.

Lat	Lon	N_0 $10^{-6}\,\mathrm{GeV^{-1}cm^{-2}s^{-1}sr^{-1}}$	n	$E_{\rm cut}$ GeV	$2\Delta\log\mathcal{L}$	$E_{\rm cut,95\%}$ GeV	$E^{\rm min}_{\rm cut,95\%}$ GeV
$(2°, 6°)$	$(0°, 10°)$	1.5 ± 0.3	1.9 ± 0.1	45 ± 17	4.8	25	25
	$(-10°, 0°)$	3.1 ± 0.4	2.2 ± 0.05	–	< 0.1	510	510
$(-2°, 2°)$	$(0°, 10°)$	6.4 ± 1.1	2.3 ± 0.09	–	< 0.1	300	2.4
	$(-10°, 0°)$	7.9 ± 0.7	2.1 ± 0.04	–	< 0.1	1000	600
$(-6°, -2°)$	$(0°, 10°)$	2.5 ± 0.4	2.1 ± 0.07	260 ± 150	3.8	130	2.3
	$(-10°, 0°)$	4.0 ± 0.3	2.2 ± 0.04	–	< 0.1	560	560

4.4. IC model of the gamma-ray emission

In this section we model the gamma-ray emission at the base of the FBs with an IC scattering model. The SED of the gamma-ray intensity is parametrized as

$$E_\gamma^2 \frac{dF_\gamma}{dE_\gamma} = \frac{E_\gamma c}{4\pi} \int \frac{\mathrm{d}n_{h\nu}}{\mathrm{d}E_{h\nu}} \sigma_{\rm IC} \frac{\mathrm{d}\Sigma_{\rm e}}{\mathrm{d}E_{\rm e}} \mathrm{d}E_{h\nu}\,\mathrm{d}E_{\rm e}, \qquad (7)$$

where $\frac{\mathrm{d}\Sigma_{\rm e}}{\mathrm{d}E_{\rm e}} = \int \frac{\mathrm{d}n_{\rm e}}{\mathrm{d}E_{\rm e}} dR$ is the column density of CR electrons integrated along the line-of-sight distance

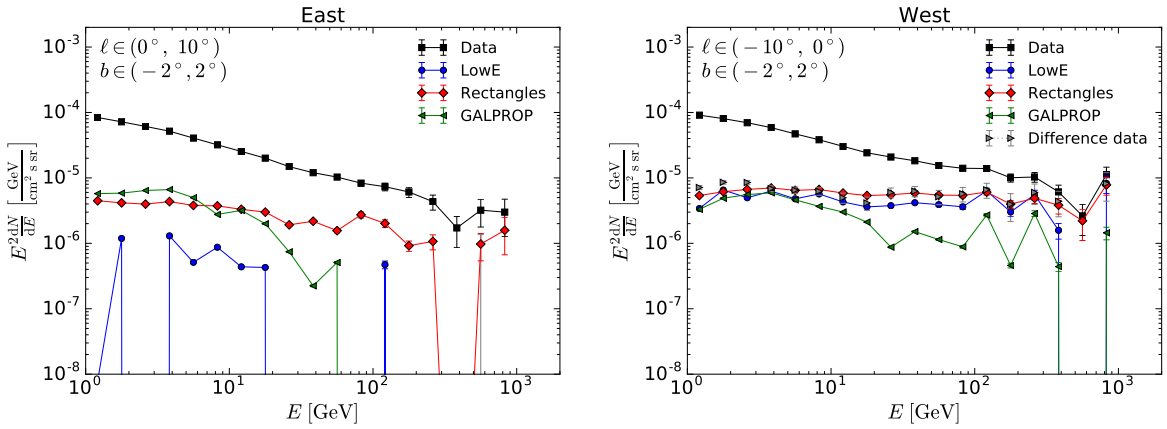


Fig. 9: SEDs of the gamma-ray data, of the residuals ("LowE" model), rectangles model of the FBs ("rectangles" model), residuals plus FBs model plus gNFW DM annihilation template ("GALPROP" model), and of the difference in the data west minus east of the GC (excluding pixels in the PS mask).

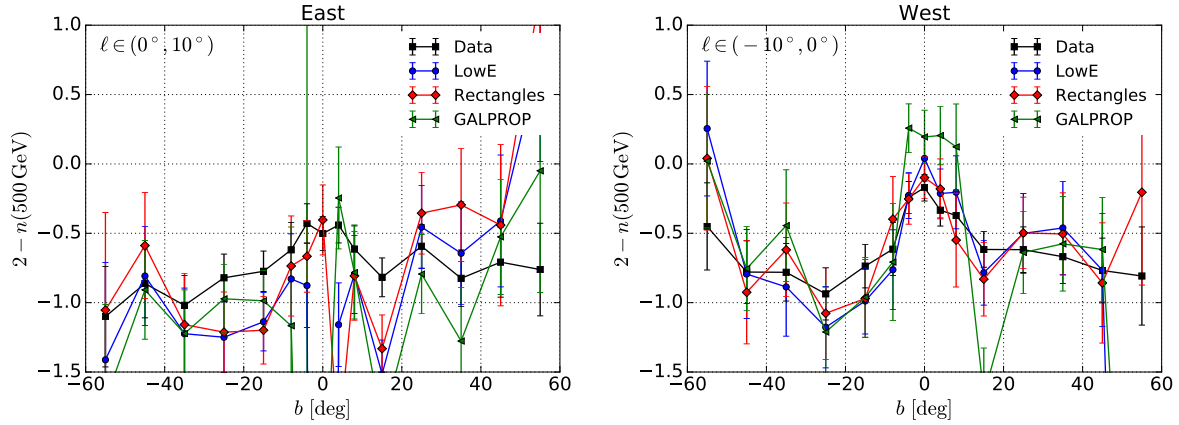


Fig. 10: Index of the log-parabola defined in Equation (5) at $E = 500\,\mathrm{GeV}$ as a function of latitude for the FBs in the different foreground diffuse emission models.

R, $\frac{\mathrm{d}n_{h\nu}}{\mathrm{d}E_{h\nu}}$ is the number density of ISRF photons of energy $h\nu$, and $\sigma_{\mathrm{IC}}(E_\gamma, E_{h\nu}, E_\mathrm{e})$ is the differential IC scattering cross section in units of $E_\gamma \frac{d\sigma}{dE_\gamma}$ (Blumenthal & Gould 1970). For details on the parametrization of σ_{IC} see Appendix B of Ackermann et al. (2014). The ISRF number density for SL and IR photons is taken from Porter et al. (2008) (available with the distribution of GALPROP v54.1), assuming that the emission at the base of the FBs is near the GC. For the CMB, we use the thermal spectrum with a temperature of 2.73 K. There is a significant uncertainty in the Galactic ISRF energy density near the GC (e.g., Popescu et al. 2017; Porter et al. 2017; Niederwanger et al. 2019). We find (Appendix C) that this uncertainty can lead to a factor ~ 3 uncertainty in the overall normalization of the inferred CR electrons (CRe) energy density. Additional uncertainty on the CRe distribution and the associated IC emission comes from the distribution of the Galactic magnetic field (e.g., Orlando 2018, 2019). We model the column density of electrons as a power law with a cutoff

$$\frac{\mathrm{d}\Sigma_\mathrm{e}}{\mathrm{d}E_\mathrm{e}} = n_\mathrm{e} \left(\frac{E_\mathrm{e}}{1\,\mathrm{GeV}}\right)^{-\gamma_\mathrm{e}} e^{-E_\mathrm{e}/E_\mathrm{cut}}. \quad (8)$$

In order to determine the normalization n_e, the spectral index γ_e, and the cutoff E_cut, we fit the IC model of the FBs plus the (fixed) foreground model counts to the total smoothed gamma-ray counts in different latitude stripes using likelihood based on the gamma distribution. As a baseline case, we take the gamma-ray spectrum derived in the rectangles model of the FBs in Section 3.3. The best-fit spectra for the rectangles model of the bubbles are shown in Figure 11 in latitude stripes $b \in (2^\circ, 6^\circ)$, $b \in (-2^\circ, 2^\circ)$ and $b \in (-6^\circ, -2^\circ)$. If the improvement in $2\Delta \log \mathcal{L}$ with and without the cutoff is less

than 0.1, then we show only the parameters for the power-law model without a cutoff. For example, for negative longitudes the cutoff is not significant.

The 95% statistical lower limit on the cutoff energy for the rectangles model and the minimum among the three models presented in Sections 3.2 – 3.4 of the 95% confidence lower limits for the cutoff energy are presented in Table 2. For negative longitudes, the 95% confidence lower limit on the cutoff in the spectrum of electrons in the rectangles model is about 4 TeV, while the minimal value of the 95% confidence limit for the three models of the foreground emission is about 3 TeV.

4.5. Hadronic model of gamma-ray emission

In the hadronic model, the gamma rays are produced as a result of collisions of hadronic CR with the interstellar gas. The gamma-ray intensity in the hadronic model is parametrized as

$$E_\gamma^2 \frac{dF_\gamma}{dE_\gamma} = \frac{E_\gamma}{4\pi} \int n_{\rm H}\ \sigma_{\rm p} v_{\rm p} \left(\frac{{\rm d}\Sigma}{{\rm d}T}\right)_{\rm p} {\rm d}T_{\rm p}, \qquad (9)$$

where $\left(\frac{{\rm d}\Sigma}{{\rm d}T}\right)_{\rm p} = \int \left(\frac{{\rm d}n}{{\rm d}T}\right)_{\rm p} dR$ is the column density of CR protons, $v_{\rm p}$ is the velocity of the protons, $T_{\rm p} = \sqrt{(qc)^2 + (m_p c^2)^2} - m_p c^2$ is the kinetic energy of the protons as a function of momentum q, $\sigma_{\rm p}(E_\gamma, T_{\rm p})$ is the differential cross section in units of $E_\gamma \frac{d\sigma}{dE_\gamma}$ for gamma rays in proton-proton collisions (Kamae et al. 2006; Karlsson & Kamae 2008), and $n_{\rm H}$ is the density of gas. We will use $n_{\rm H} = 1\,{\rm cm}^{-3}$ as a reference density, which is comparable with the gas surface density of $\sim 30 M_\odot {\rm pc}^{-2}$ (Miville-Deschênes et al. 2017) averaged over the approximate height of the enhanced emission at the base of the bubbles, e.g., ~ 900 pc above and below the GC. Since most of the gas density is concentrated within 100 – 200 pc from the midplane (e.g., Sofue 2013; Miville-Deschênes et al. 2017), the gas density in the plane near the GC is 5 – 10 cm^{-3}, which is consistent with the enhancement of the intensity of the emission at the base of the FBs at $\ell = 0°$. We model the proton spectrum as a power law of the momentum $\frac{d\Sigma}{dqc} = n_{\rm p} q^{-\gamma_p}$ (note, that $v_{\rm p} \frac{{\rm d}\Sigma}{{\rm d}T_{\rm p}} = c \frac{d\Sigma}{dqc}$).

We fit the hadronic model of the gamma-ray emission at the base of the FBs analogously to the leptonic model in Section 4.4. The dash-dotted line in Figure 11 represents the best-fit hadronic spectrum (labeled as π^0). The index of the proton spectrum is relatively hard $\gamma_{\rm p} \lesssim 2.3$, especially to the west of the GC.

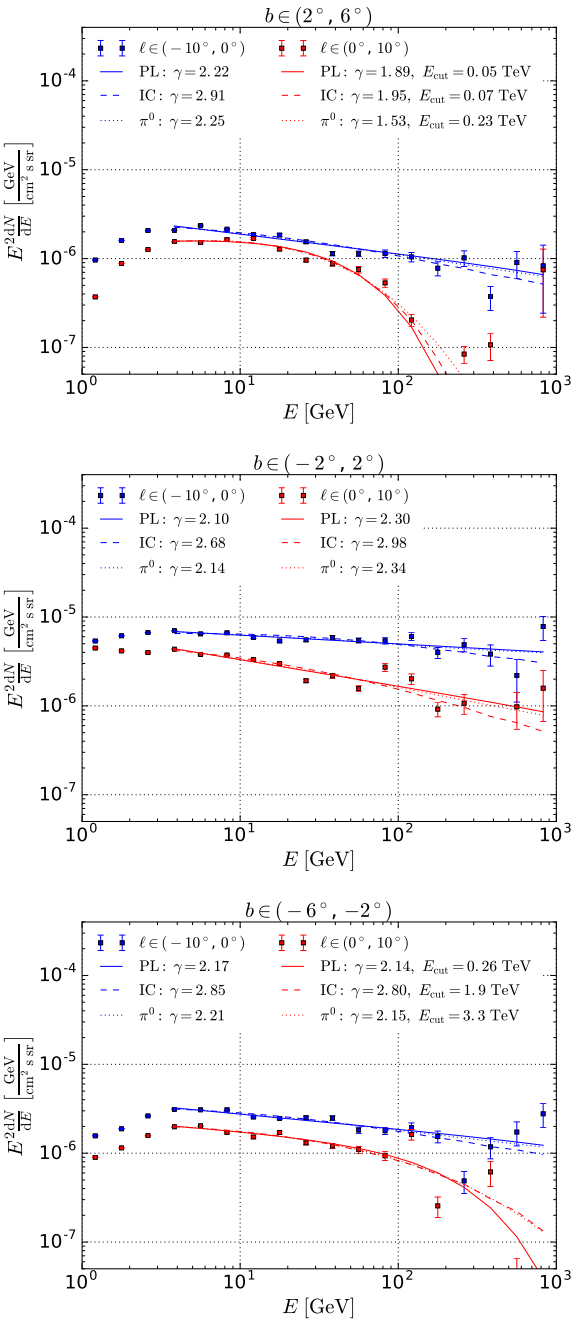


Fig. 11: SEDs of the rectangles model of the FBs in the latitude stripes $(2°, 6°)$, $(-2°, 2°)$ and $(-6°, -2°)$ for negative (blue) and positive (red) longitudes. We compare the parametric model of the SED with the leptonic (Section 4.4) and the hadronic (Section 4.5) models.

We calculate the significance of a cutoff in the CR proton spectrum by adding an exponential cutoff factor and refitting the model to the gamma-ray data. The improvement in the model and the 95% confidence lower bound on the cutoff values are presented in Table 3. Within ±6° from the Galactic plane west of the GC, the 95% confidence level for the lower bound on the cutoff among the models of

Table 2: Energy cutoff values and the significance of the cutoff in the IC model of the FBs at low latitudes. The lower bounds for $E_{\rm cut}$ at the 95% confidence level for our baseline model and the minimum among the models presented in Sections 3.2 – 3.4 are shown in the last two columns respectively.

Lat	Lon	$2\Delta \log \mathcal{L}$	Lower bound on $E_{\rm cut}$ (TeV)	
			Rectangles model	All models
$(2°, 6°)$	$(0°, 10°)$	2.6	0.20	0.17
	$(-10°, 0°)$	< 0.1	4.0	4.0
$(-2°, 2°)$	$(0°, 10°)$	< 0.1	1.4	0.01
	$(-10°, 0°)$	< 0.1	13	2.9
$(-6°, -2°)$	$(0°, 10°)$	1.1	0.82	0.03
	$(-10°, 0°)$	< 0.1	7.0	7.0

the foreground emission that we have considered in Sections 3.2 – 3.4 is about 6 TeV.

4.6. Summary of the spectral analysis

In Figure 12 we show the envelopes of the gamma-ray spectra at $|b| < 2°$ of the emission at the base of the FBs for the models of foreground emission that we have considered, including the models where we change the selection of the low energies in the definition of the foreground emission model (Appendix A). In order to determine the maximal and minimal models of the FBs in the Galactic plane, we fit the maximal and minimal points in the envelope above 3 GeV with a power law with a cutoff function (we fit above 3 GeV because some of the models of the foreground emission in Appendix A are determined for energies between 1 and 2.2 GeV). The corresponding parameters are reported in the first row of Table 4. We also fit the IC and hadronic models to the maximal and minimal points in the envelope and report the corresponding parameters in Table 4.

5. Intepretation

The bright and hard gamma-ray emission at the base of the bubbles can be at any position along the line of sight. In this section we consider two characteristic scenarios: that the emission is near the GC or that the emission is produced by one or a few SNRs closer to us.

5.1. Emission near the GC scenario

In the estimates in this subsection we use the following characteristic sizes: the distance to the GC is 8.5 kpc, the size of the region with the enhanced gamma-ray emission interpreted as an additional population of CR: $-10° < \ell < 0°$ and $|b| < 6°$. If we assume that the geometry of the region is a simple box, then the size of the box along the GP is 1.5 kpc, while the half-size in the vertical direction (distance from the GP to the boundary) is $\Delta h = 0.9$ kpc. The total gamma-ray luminosity in this case can be estimated by summing the data points in the rectangles model in Figure 11 for $|b| < 6°$, which yields the luminosity of $L = 1.1 \times 10^{37}$erg s^{-1} above 1 GeV.

One of the most intriguing features of the gamma-ray spectrum at the base of the FBs is the absence of a significant cutoff up to 1 TeV and an inferred hard spectrum of underlying electrons or protons. In particular, if the emission originates in hadronic interactions, the spectrum of the CR protons (CRp) is $\sim E^{-2.2}$ which is significantly harder than the propagated spectrum $\sim E^{-2.5-2.7}$ observed both locally (e.g., Casandjian 2015; Remy et al. 2017; Neronov et al. 2017; Prokhorov & Colafrancesco 2018) and throughout the Galactic plane (e.g., Gaggero et al. 2015; Acero et al. 2016; Yang et al. 2016; Aharonian et al. 2018). Although there is a hardening of the spectrum of CR in the inner rings of the Galaxy and near the GC, the inferred spectra of the CR at the base of the FBs are significantly harder than the propagated spectra of the CR in the inner rings and near the GC (Gaggero et al. 2015; Acero et al. 2016; Yang et al. 2016; Aharonian et al. 2018). We assume that the CRp spectrum at the base of the bubbles is equal to the injection spectrum unaffected by the propagation softening. This is possible if the CRp were injected relatively recently and had insufficient time to escape from the region of the enhanced emission, i.e., the age of the CRp is less than the propagation time to cross the vertical distance of 0.9 kpc. If we assume a spatially constant diffusion coefficient $D(E) = D_0 \left(\frac{E}{1\,\rm GeV}\right)^{\delta}$ with $D_0 = 3 \times 10^{28}\,{\rm cm}^2/{\rm s} = 100\,{\rm pc}^2/{\rm kyr}$ and $\delta = 0.4$

Table 3: Energy cutoff values and the significance of the cutoff in the hadronic model of the FBs at low latitudes. The lower bounds for $E_{\rm cut}$ at the 95% confidence level for our baseline model and the minimum among the models presented in Sections 3.2 – 3.4 are shown in the last two columns respectively.

lat	lon	$2\Delta \log \mathcal{L}$	Lower bound on $E_{\rm cut}$ (TeV)	
			Rectangles model	All models
$(2°, 6°)$	$(0°, 10°)$	4.4	0.88	0.48
	$(-10°, 0°)$	< 0.1	7.4	7.4
$(-2°, 2°)$	$(0°, 10°)$	< 0.1	3.8	0.023
	$(-10°, 0°)$	< 0.1	29	6.3
$(-6°, -2°)$	$(0°, 10°)$	2.7	1.6	0.05
	$(-10°, 0°)$	< 0.1	12	12

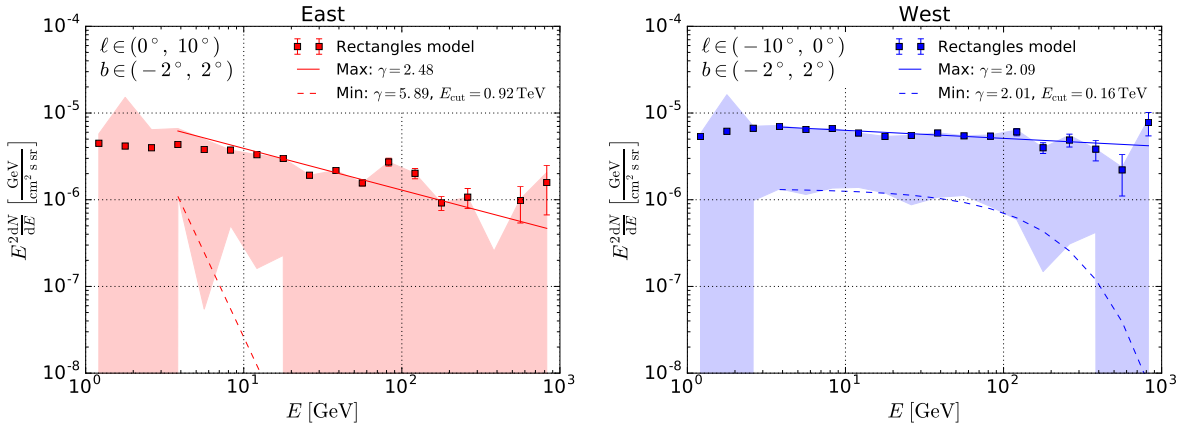


Fig. 12: SED of the FBs in the Galactic plane. The shaded areas show the envelope of the FB's spectra in all foreground models considered in the paper including the changes in the choice of the low-energy range to model the foreground emission (discussed in Appendix A). The lines show the fits to the maximal and minimal points in the envelopes above 3 GeV.

Table 4: Summary of the min and max models for the parametric, IC and hadronic models of the FBs for $|b| < 2°$ and $-10° < \ell < 0°$. For the parametric model, we report the energy spectrum of the gamma rays, for the IC model we report the column density of the electrons' spectrum as a function of energy, while for the hadronic model – the column density of the protons' spectrum as a function of momentum. The spectra are normalized at $E_0 = 1$ GeV. The last column shows the statistical 95% confidence lower limit on the cutoff, $E_{\rm cut,95\%}$.

Model	Type	norm	index	cutoff TeV	$E_{\rm cut,95\%}$ TeV
Parametric, $\frac{dN_\gamma}{dE}$ $[\mathrm{GeV}^{-1}\,\mathrm{cm}^{-2}\,\mathrm{s}^{-1}]$	max	7.8×10^{-6}	2.09	–	0.99
	min	1.4×10^{-6}	2.01	0.16	0.04
IC, $\frac{d\Sigma_e}{dE}$ $[\mathrm{GeV}^{-1}\,\mathrm{cm}^{-2}]$	max	3.4×10^{10}	2.67	–	19
	min	1.3×10^{10}	2.81	7.2	0.96
Hadronic, $\frac{d\Sigma_p}{dqc}$ $[\mathrm{GeV}^{-1}\,\mathrm{cm}^{-2}]$	max	9.5×10^{11}	2.13	–	65
	min	1.1×10^{11}	1.98	1.8	0.23

(Strong et al. 2007), then the escape time for the protons at $E > 6\,\mathrm{TeV}$ is

$$T_{\rm esc} < \frac{\Delta h^2}{2D(E)} \approx 100\,\mathrm{kyr}. \quad (10)$$

This gives us an approximate upper bound on the age of the proton CR, assuming that the diffusion coefficient near the GC is similar to the diffusion coefficient near Sun. The escape time can be significantly longer, if the diffusion length near the GC is smaller than the local one or if the CR are confined by a particular configuration of magnetic fields. The CRp energy density within $|b| < 6°$ in the rectangles model of the FBs (Section 4.5) normalized to the reference density of $n_{\rm H} = 1\,\mathrm{cm}^{-3}$ is $\mathrm{d}E_{\rm tot}/\mathrm{d}V = 360\,\mathrm{meV\,cm}^{-3}$ above 1 GeV. In Figure 13 (left), we compare the corresponding flux to

the local CRp flux. The total energy in CRp within $|b| < 6^\circ$ is $E_{\rm tot} = 7 \times 10^{52}$ erg. This population of CRp can be obtained from ~ 700 SNe, assuming that on average SNe inject $\sim 10^{50}$ erg in CRp, which corresponds to about 10% efficiency of CR acceleration by a SN with kinetic energy $\sim 10^{51}$ erg (e.g., Spurio 2015). There are several populations of young stellar objects near the GC (Yusef-Zadeh et al. 2009; Immer et al. 2012), in particular there is a population of stars close to the GC with an age of about 6 Myr (Paumard et al. 2006). If we assume that the rate of SNe in the Galaxy is about one per century and that the GC region contributes at the level of a few percent to the total rate, e.g., a few SNRs per 10 kyr, then the 700 SNRs can be produced near the GC in the past few million years.

The best-fit spectrum of CRe is $\sim E^{-2.7}$, which is softer than the spectrum of the protons. Nonetheless, this spectrum is harder than the spectrum expected in the presence of cooling for a stationary population of CRe. Thus, unless the injection spectrum is harder than E^{-2}, the population of the CRe at the base of the bubbles is not affected by cooling up to 3 TeV, which is the 95% confidence minimal lower bound on the cutoff in the CRe (Table 2). The cooling time for the electrons at 3 TeV is $T_{\rm cool} \approx 200$ kyr, which is comparable to the diffusive escape time from the ± 900 pc volume around the GP at 3 TeV. The cooling time can have a factor ~ 3 uncertainty due to the uncertainties in the ISRF near the GC (see Appendix C).

The energy density in electrons with energies above $E_0 = 1$ GeV, which is necessary to produce the gamma-ray emission in the rectangles model of the FBs (Section 4.4), is 4.0 meV cm^{-3}. In Figure 13 (right), we compare the corresponding flux to the local CRe flux. The total energy content of the ROI in electrons above 1 GeV is $E_{\rm tot} = 3 \times 10^{51}$ erg, which corresponds to the CR energy output of 3000 SNe assuming a 0.1% efficiency in converting the SNR kinetic energy to CRe energy. The ratio of the electron and proton acceleration efficiencies $K_{e/p} = 10^{-2}$ assumed here is relatively optimistic, given that the ratio of efficiencies can be as low as $\sim 10^{-3}$ (e.g., Park et al. 2015). Similar efficiencies of $K_{e/p} \propto 10^{-2}$ can be expected in the acceleration of electrons and protons in jets from supermassive black holes (e.g., Ball et al. 2018). Since the escape time is comparable to the electron cooling time and the required number of SNe in the hadronic scenario is smaller than the number of SNe in the leptonic scenario (for the ratio of acceleration efficiencies $K_{e/p} \lesssim 10^{-2}$), we conclude that the majority of the gamma-ray emission near the base of the FBs is likely to be produced by the hadronic interactions of CRp with the gas. The presence of the hadronic production of gamma rays at the base of the FBs, without any sign of a cutoff up to gamma-ray energies of 1 TeV, is important for the detectability of the associated neutrino signal by neutrino telescopes, Figure 14 (see also Razzaque & Yang 2018).

5.2. A nearby SNR or a superbubble scenario

In this subsection we discuss models where the hard and bright gamma-ray emission at the base of the FBs is created either by a single SNR or several SNRs at a distance closer than the distance to the GC. We start with a single SNR scenario. For the leptonic model we use the local ISRF and calculate the IC emission as described in Section 4.4. Assuming one SNR, we find a distance of 50 pc. The radius of an SNR corresponding to 6° circle at a distance of 50 pc is about 5 pc. Provided that the SNR would be rather close to Earth, it should be detected in radio and X-ray observations, however no suitable candidates are currently known (Green 2014, 2017). For the hadronic model of the gamma-ray emission, we assume the local gas density of 1 cm^{-3}. At the GC, we need about 700 SNRs for this reference gas density; thus the distance where a single SNR can explain the excess emission is $d = \frac{8.5 \text{ kpc}}{\sqrt{700}} \approx 300$ pc. We can compare the flux from the low-latitude bubbles with the emission of a known SNR, such as Tycho's SNR. The differential energy flux of Tycho's SNR at 10 GeV is $E^2 dF/dE \approx 10^{-6}$ MeV cm^{-2}s^{-1} (Archambault et al. 2017). The solid angle of the ROI of $10^\circ \times 12^\circ$ at the base of the FBs is $\Omega \approx 0.037$ sr. If we assume that Tycho's SNR is at a distance of 3 kpc, then the average intensity inside Ω at a distance of 300 pc is $E^2 dN/dE \approx 2.7 \times 10^{-6}$ GeV cm^{-2}s^{-1}sr^{-1}, which is comparable to the FBs emission at latitudes $|b| < 6^\circ$ (e.g., Figure 12). The radius of Tycho's SNR is about 3.5 pc (for the angular diameter of $8'$ at 3 kpc), while the radius corresponding to 6° angular size at 300 pc is about 30 pc, which is almost 10 times larger than the radius of Tycho's SNR. If we assume that only the core of the emission at the base of the FBs within $|b| < 2^\circ$ corresponds to an SNR, the corresponding linear size is ≈ 10 pc (for the same distance of 300 pc). There are several SNRs in Green's catalog (Green 2014, 2017)

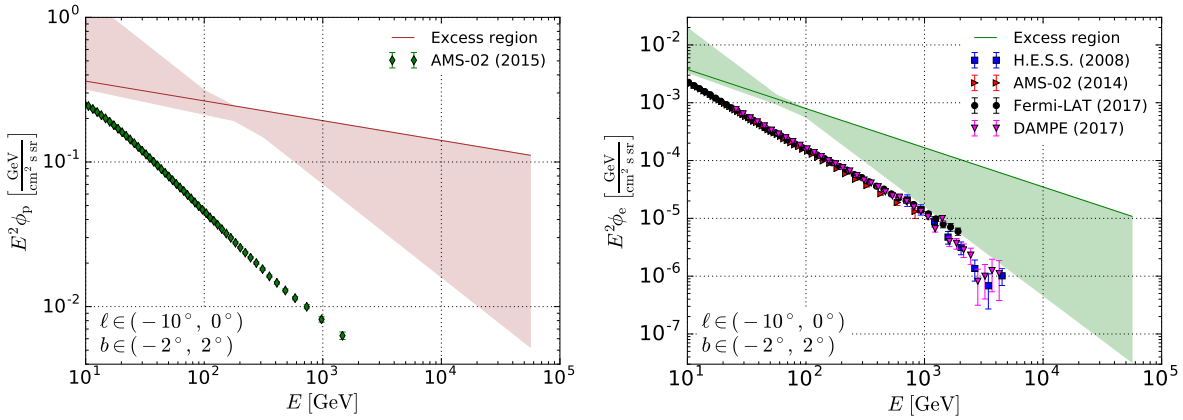


Fig. 13: Proton (left) and electron (right) spectra fitted to the gamma-ray emission at the base of the FBs. Solid lines show the best-fit spectra in the rectangles model of the FBs. The shaded bands represent the systematic uncertainties, estimated from the maximal and minimal best-fit FBs spectra among the foreground models. Uncertainties in the ISRF energy density near the GC result in an additional factor of ~ 2 uncertainties in the CRe energy density (see Appendix C for details). For comparison with the local CR spectrum, we show the local fluxes of CRp measured by AMS-02 (Aguilar et al. 2015) and CRe measured by H.E.S.S. (Aharonian et al. 2008), AMS-02 (Aguilar et al. 2014), *Fermi*-LAT (Abdollahi et al. 2017), and *DAMPE* (Ambrosi et al. 2017). The error bars represent the systematic and statistical uncertainties added in quadrature.

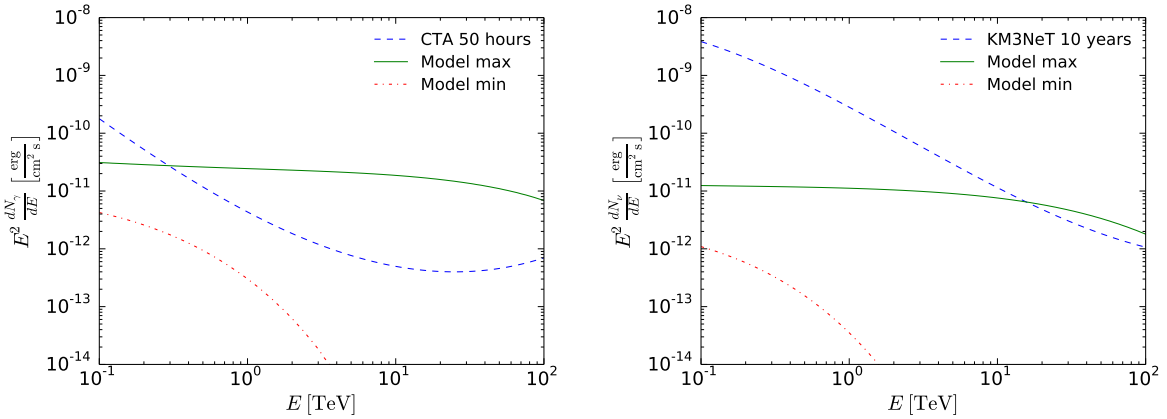


Fig. 14: Comparison of the hadronic model of the gamma-ray emission at the base of the FBs with the sensitivities of CTA and KM3NeT for a source with 2° radius (Ambrogi et al. 2018). The min and max models correspond to the min and max models in the hadronic scenario in Table 4 (for the max model we assume a cutoff in the proton spectrum at 1 PeV) integrated over a 2° circle to transform intensity to flux. The KM3NeT sensitivity is for muon neutrinos only. In estimating the sensitivity, we take into account that the GC is below the horizon for about 2/3 of the time at the KM3NeT location in the Mediterranean Sea.

between $-10^\circ < \ell < 0^\circ$, but all of them have relatively small angular diameters $\lesssim 30'$. Thus a single SNR is not a plausible scenario for the emission at the base of the FBs, unless this SNR is missing in Green's catalog.

Another possibility is that the emission at the base of the FBs is created by several SNRs and / or wind from massive stars, similar to the Cygnus cocoon (Ackermann et al. 2011) or the Loop I and the local superbubbles (Smith & Cox 2001; Breitschwerdt & de Avillez 2006; Wolleben 2007; Breitschwerdt et al. 2016; Schulreich et al. 2018; Dickinson 2018; Shchekinov 2018). The Cygnus cocoon (Ackermann et al. 2011) has a radius of about 2°, which at a distance of 1.4 kpc, corresponds to a radius of about 50 pc. If a Cygnus-like region is responsible for the emission within $|b| < 6^\circ$ at the base of the FBs, then such region should be at a distance of about 500 pc. If only the core of the high-intensity region within $|b| < 2^\circ$ is explained by such a cocoon,

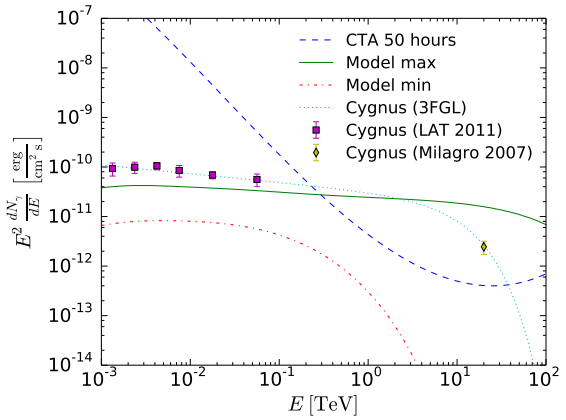


Fig. 15: Comparison of the min and max models of the residual flux at the base of the FBs with the Cygnus cocoon spectrum. The min and the max models are the same as in Figure 14. For the 3FGL spectrum we take the power-law parameters from the catalog (Acero et al. 2015) and add a cutoff in the gamma-ray spectrum at 10 TeV so that the SED is consistent with the Milagro source MGRO J2031+41 at 20 TeV (Abdo et al. 2007). The purple squares represent the measurement of the flux from the Cygnus cocoon by the *Fermi*-LAT collaboration (Ackermann et al. 2011).

then the distance would be similar to the distance to the Cygnus cocoon, i.e., about 1.4 kpc. In Figure 15 we compare the gamma-ray intensity at the base of the FB integrated over a 2° circle to the flux from the Cygnus cocoon (Abdo et al. 2007; Ackermann et al. 2011). The flux in the max model is comparable (within a factor of 2) to the flux from the Cygnus cocoon between 1 and 100 GeV.

Massive stars, which can inflate cocoons or superbubbles by stellar winds and SN explosions, are usually found in young open stellar clusters. There are several young open stellar clusters in the direction of the base of the FBs, i.e., within $-10° < \ell < 0°$. For example, clusters Trumpler 27 (Moffat et al. 1977) or NGC 6383 (Lloyd Evans 1978) contain more than 10 massive OB stars, have an age of about 10 Myr, and an estimated distance of 1.2 kpc and 1 kpc, respectively, in the direction of $\ell \approx 356°$, $b \approx 0°$. There is also a cluster NGC 6405 (Rohlfs et al. 1959), which has a smaller estimated distance of about 500 pc but an older age ~ 100 Myr. The turbulence created by winds from the massive stars as well as the past SNRs in these clusters can (re)accelerate cosmic rays and it would also lead to smaller diffusion length, which would prevent the escape of CR on timescales shorter than a few Myr (Ackermann et al. 2011). There are relatively few SNRs detected in gamma rays in that area of the sky. In particular, there is only one SNR, 3FGL J1741.1−3053, in the 3FGL catalog (Acero et al. 2015) between $-10° < \ell < 0°$. This SNR is associated with the Tornado nebula at a distance of 12 kpc (Castro et al. 2013). Green's catalog of SNRs contains several SNRs between $-10° < \ell < 0°$, but SNRs with measured distances are more than 4 kpc away. The absence of detected SNRs in the direction of the base of the FBs at distances $\lesssim 1.5$ kpc does not necessarily mean that there were no SNRs in the open clusters mentioned above. A possible reason is that the wind from the massive stars as well as the first SNRs in the cluster create a hot superbubble with smaller gas density than the average density in the Galactic plane. As a result, the subsequent SNRs quickly expand in the less dense environment until they reach the common envelope of the superbubble. For instance, this is observed in simulations of the formation of the local hot superbubble (Breitschwerdt et al. 2016; Schulreich et al. 2017, 2018). Whether the stellar clusters can provide the necessary CR injection rate to power the gamma-ray emission at the base of the FBs deserves a separate detailed study.

An interesting question is whether the FBs themselves can be inflated by a Cygnus-like superbubble, which accidentally happened along the line of sight towards the GC. If the FBs are at a distance of about 1 kpc, then their vertical size is also about 1 kpc, which is 10 times smaller than the size of the FBs at a distance of 8.5 kpc. In the leptonic scenario of the FBs, the 10^{52} erg in CRe at 8.5 kpc (Ackermann et al. 2014) would correspond to 10^{50} erg at 1 kpc. This power can be provided by several hundred SNe, which is a relatively large number, given the few young stellar clusters at distances $\lesssim 1$ kpc in the direction of the base of the FBs. This estimate is based on an assumed 0.1% efficiency in acceleration of CRe by SN shells; if there is an additional acceleration of the electrons by the turbulence either at the base of the FBs or inside the high-latitude FB volume, then the required number of SNRs would be smaller.

The electrons can be delivered to the FBs volume by an outflow, possibly, created by the pressure of the CR themselves (e.g., Jacob et al. 2018). The measured red- and blue-shift velocities of the gas outflow in the direction of the FBs are about 200 – 300 km/s, which imply the gas outflow from the Galactic plane in a biconical model of the FBs

with velocities $\gtrsim 900$ km/s and an age of the outflow at the position above the GC about 6 – 9 Myr (Fox et al. 2015; Bordoloi et al. 2017). If the distance is 10 times smaller, then the age would be $\sim 600 - 900$ kyr, which is comparable to the cooling time of 1 TeV electrons necessary to explain the gamma-ray emission from the FBs at high latitudes (Ackermann et al. 2014). Thus the gamma-ray emission at high latitudes could be explained by an IC model with about 100 SNRs (or fewer if there is re-acceleration of electrons) created ~ 1 Myr ago, while the bright and hard emission at the base of the bubbles can be explained by the hadronic emission from about 10 SNRs. The actual age of the CR is determined by the confinement within the superbubble and can be also on the order of 1 Myr or more. In this scenario, the star-forming region, which can power the emission at the base of the FBs and, possibly, the FBs themselves can be situated in the Sagittarius arm at a distance of 1 – 1.5 kpc in the direction of the GC.

6. Conclusions

In this paper we use 9 years of *Fermi*-LAT Pass 8 Source class data to study the gamma-ray emission at the base of the FBs. We use different methods to construct the foreground diffuse gamma-ray components and to determine the properties of the residual gamma-ray emission at the base of the FBs. We confirm the earlier findings that the emission at the base of the FB has a higher intensity than the FBs emission at high latitudes. The spectrum at the base of the FBs is consistent with a single power law without a cutoff up to about 1 TeV. The emission is slightly displaced from the GC to negative longitudes, which favors a starburst scenario of the bubbles formation, unless there is a mechanism to shift the gamma-ray emission away from Sgr A* in the SMBH scenario.

The gamma-ray emission at the base of the FBs can be explained by either a hadronic or a leptonic model of gamma-ray production with CR spectra consistent with a power law without a cutoff. The index of the CRe (CRp) spectrum is 2.6 – 2.9 (2.0 – 2.3). We derive the 95% confidence lower bound on the cutoff in the CR electron and proton spectra by selecting the lowest 95% statistical confidence value among the models of the foreground emission considered in Sections 3.2 – 3.4. Within $|b| < 6^\circ$ and $-10^\circ < \ell < 0^\circ$, the 95% confidence lower bound on the exponential cutoff in the CRe (CRp) spectrum is about 3 (6) TeV.

If the location of the residual emission is near the GC, then the total gamma-ray luminosity is $L \approx 10^{37}$ erg s^{-1} and the required energy of CRe (CRp) above 1 GeV is $E_{\rm e} = 3 \times 10^{51}$ erg ($E_{\rm p} = 7 \times 10^{52}$ erg). Although the total required energy in CRe is smaller than in CRp, the efficiency of acceleration of hadronic CR is expected to be significantly higher than for leptonic CR. In particular, with 10% CRp acceleration efficiency, one needs about 700 SNRs to explain the gamma-ray emission in the hadronic scenario near the GC, while with 0.1% CRe acceleration efficiency, the required number of SNRs is 3000. For the GC scenario, the estimated diffusive escape time and the electron cooling time is ~ 100 kyr. In this case one needs a relatively high SN rate of one per ~ 100 yr at the location of the gamma-ray emission. If the average ISRF energy density is a factor of ~ 2 lower or higher than the ISRF in the reference model (Appendix C), then both the cooling time and the required energy density of CRe will be a factor of ~ 2 higher or lower than in the reference model, which nevertheless requires the same SN rate of one per ~ 100 yr.

If the residual gamma-ray emission is produced at a closer distance, e.g., at about 1 kpc by a Cygnus-like cocoon or a superbubble in the Sagittarius arm, then the required number of SNRs is about two orders of magnitude smaller. For the superbubble scenario, the characteristic linear size is 10 times smaller, which leads to 100 times shorter diffusion time of a few kyr. This is shorter than the lifetime of individual SNRs. Both in the GC and in the superbubble scenarios, the age of the CR population can be greater than the diffusion time if there is an additional confinement by the SN shells or the shell of a superbubble.

Apart from the question of the location of the emission at the base of the FBs, one can revisit the question of the location of the FBs themselves: the FBs could have been inflated by a superbubble about 1 Myr ago at a distance of 1 kpc from the Sun. The CR in the past superbubble may create a wind with velocities up to ~ 1000 km/s, which is sufficient to inflate a 1 kpc large bubble within 1 Myr so that the CR electrons in the wind do not cool below 1 TeV and can explain the gamma-ray emission from the FBs at high latitudes. The gamma-ray emission at low latitudes is then explained (most naturally) by a hadronic scenario

from a more recent starburst episode at about the same location.

In the future, the bright and hard gamma-ray emission at the base of the FB should be detectable with CTA, or a version of the HAWC experiment in the southern hemisphere (Mostafa et al. 2017; Assis et al. 2017; Razzaque & Yang 2018). Observations with Cherenkov telescopes should detect or constrain the cutoff energy in the gamma-ray spectrum in multi-TeV regime. In the hadronic scenario, for a sufficiently high cutoff value of the CRp spectrum, e.g., around 1 PeV, the corresponding neutrino emission could be detected with the future KM3NeT telescope.

Acknowledgements

The authors would like to thank Seth Digel, Anna Franckowiak, Stefan Funk, Gudlaugur Johannesson, Tsunefumi Mizuno, Troy Porter, Andrew Strong, and Luigi Tibaldo for valuable comments and suggestions. Also we would like to thank Cristina Popescu for providing us the ISRF data files in fits format. The Fermi LAT Collaboration acknowledges generous ongoing support from a number of agencies and institutes that have supported both the development and the operation of the LAT as well as scientific data analysis. These include the National Aeronautics and Space Administration and the Department of Energy in the United States, the Commissariat à l'Energie Atomique and the Centre National de la Recherche Scientifique / Institut National de Physique Nucléaire et de Physique des Particules in France, the Agenzia Spaziale Italiana and the Istituto Nazionale di Fisica Nucleare in Italy, the Ministry of Education, Culture, Sports, Science and Technology (MEXT), High Energy Accelerator Research Organization (KEK) and Japan Aerospace Exploration Agency (JAXA) in Japan, and the K. A. Wallenberg Foundation, the Swedish Research Council and the Swedish National Space Board in Sweden.

References

Abazajian, K. N., Canac, N., Horiuchi, S., & Kaplinghat, M. 2014, Phys. Rev. D, 90, 023526
Abdo, A. A., Ackermann, M., Ajello, M., et al. 2011a, ApJ, 734, 28
Abdo, A. A., Ackermann, M., Ajello, M., et al. 2011b, ApJ, 734, 116
Abdo, A. A., Allen, B., Berley, D., et al. 2007, ApJ, 664, L91
Abdollahi, S., Ackermann, M., Ajello, M., et al. 2017, Phys. Rev. D, 95, 082007
Acero, F., Ackermann, M., Ajello, M., et al. 2015, ApJS, 218, 23
Acero, F., Ackermann, M., Ajello, M., et al. 2016, ApJS, 223, 26
Ackermann, M., Ajello, M., Albert, A., et al. 2016, Phys. Rev. D, 93, 082001
Ackermann, M., Ajello, M., Albert, A., et al. 2017, ApJ, 840, 43
Ackermann, M., Ajello, M., Allafort, A., et al. 2011, Science, 334, 1103
Ackermann, M., Albert, A., Atwood, W. B., et al. 2014, ApJ, 793, 64
Aguilar, M., Aisa, D., Alpat, B., et al. 2014, Physical Review Letters, 113, 221102
Aguilar, M., Aisa, D., Alpat, B., et al. 2015, Physical Review Letters, 114, 171103
Aharonian, F., Akhperjanian, A. G., Barres de Almeida, U., et al. 2008, Physical Review Letters, 101, 261104
Aharonian, F., Peron, G., Yang, R., Casanova, S., & Zanin, R. 2018, arXiv e-prints, arXiv:1811.12118
Ambrogi, L., Celli, S., & Aharonian, F. 2018, Astroparticle Physics, 100, 69
Ambrosi, G., An, Q., Asfandiyarov, R., et al. 2017, Nature, 552, 63
Archambault, S., Archer, A., Benbow, W., et al. 2017, ApJ, 836, 23
Assis, P., Barres de Almeida, U., Blanco, A., et al. 2017, ArXiv e-prints [arXiv:1709.09624]
Ball, D., Sironi, L., & Özel, F. 2018, ArXiv e-prints [arXiv:1803.05556]
Blumenthal, G. R. & Gould, R. J. 1970, Reviews of Modern Physics, 42, 237
Bordoloi, R., Fox, A. J., Lockman, F. J., et al. 2017, ApJ, 834, 191
Breitschwerdt, D. & de Avillez, M. A. 2006, A&A, 452, L1
Breitschwerdt, D., Feige, J., Schulreich, M. M., et al. 2016, Nature, 532, 73
Calore, F., Cholis, I., & Weniger, C. 2015, J. Cosmology Astropart. Phys., 3, 038
Casandjian, J.-M. 2015, ApJ, 806, 240
Castro, D., Slane, P., Carlton, A., & Figueroa-Feliciano, E. 2013, ApJ, 774, 36
Dickinson, C. 2018, Galaxies, 6, 56
Fox, A. J., Bordoloi, R., Savage, B. D., et al. 2015, ApJ, 799, L7
Freudenreich, H. T. 1998, ApJ, 492, 495
Gaggero, D., Urbano, A., Valli, M., & Ullio, P. 2015, Phys. Rev. D, 91, 083012
Goodenough, L. & Hooper, D. 2009, ArXiv:0910.2998 [arXiv:0910.2998]
Górski, K. M., Hivon, E., Banday, A. J., et al. 2005, ApJ, 622, 759

Green, D. A. 2014, Bulletin of the Astronomical Society of India, 42, 47
Green, D. A. 2017, Cavendish Laboratory, Cambridge, United Kingdom (available at "http://www.mrao.cam.ac.uk/surveys/snrs/")
Immer, K., Schuller, F., Omont, A., & Menten, K. M. 2012, A&A, 537, A121
Jacob, S., Pakmor, R., Simpson, C. M., Springel, V., & Pfrommer, C. 2018, MNRAS, 475, 570
Johannesson, G., Orlando, E., & for the Fermi-LAT collaboration. 2013, ArXiv:1307.0197 [arXiv:1307.0197]
Kamae, T., Karlsson, N., Mizuno, T., et al. 2006, ApJ, 647, 692
Karlsson, N. & Kamae, T. 2008, ApJ, 674, 278
Lloyd Evans, T. 1978, MNRAS, 184, 661
Miville-Deschênes, M.-A., Murray, N., & Lee, E. J. 2017, ApJ, 834, 57
Moffat, A. F. J., Fitzgerald, M. P., & Jackson, P. D. 1977, ApJ, 215, 106
Moskalenko, I. & Strong, A. 1998, ApJ, 493, 694
Mostafa, M., BenZvi, S., Schoorlemmer, H., Schüssler, F., et al. 2017, in APS April Meeting Abstracts, R4.005
Neronov, A., Malyshev, D., & Semikoz, D. V. 2017, A&A, 606, A22
Niederwanger, F., Reimer, O., Kissmann, R., et al. 2019, Astroparticle Physics, 107, 1
Orlando, E. 2018, MNRAS, 475, 2724
Orlando, E. 2019, arXiv e-prints [arXiv:1901.08604]
Orlando, E. & Strong, A. W. 2008, A&A, 480, 847
Park, J., Caprioli, D., & Spitkovsky, A. 2015, Physical Review Letters, 114, 085003
Paumard, T., Genzel, R., Martins, F., et al. 2006, ApJ, 643, 1011
Popescu, C. C., Yang, R., Tuffs, R. J., et al. 2017, MNRAS, 470, 2539
Porter, T. A., Jóhannesson, G., & Moskalenko, I. V. 2017, ApJ, 846, 67
Porter, T. A., Moskalenko, I. V., Strong, A. W., et al. 2008, ApJ, 682, 400
Prokhorov, D. A. & Colafrancesco, S. 2018, MNRAS, 478, 2939
Ptuskin, V., Moskalenko, I. V., Jones, F., et al. 2006, ApJ, 642, 902
Razzaque, S. & Yang, L. 2018, Galaxies, 6, 47
Remy, Q., Grenier, I. A., Marshall, D. J., & Casandjian, J. M. 2017, A&A, 601, A78
Robitaille, T. P., Churchwell, E., Benjamin, R. A., et al. 2012, A&A, 545, A39
Rohlfs, K., Schrick, K. W., & Stock, J. 1959, ZAp, 47, 15
Schulreich, M., Breitschwerdt, D., Feige, J., & Dettbarn, C. 2018, Galaxies, 6, 26
Schulreich, M. M., Breitschwerdt, D., Feige, J., & Dettbarn, C. 2017, A&A, 604, A81
Shchekinov, Y. 2018, Galaxies, 6, 62
Smith, R. K. & Cox, D. P. 2001, ApJS, 134, 283
Sofue, Y. 2013, Mass Distribution and Rotation Curve in the Galaxy, ed. T. D. Oswalt & G. Gilmore, 985
Spurio, M. 2015, Particles and Astrophysics: a Multi-Messenger Approach (Springer)
Storm, E., Weniger, C., & Calore, F. 2017, J. Cosmology Astropart. Phys., 8, 022
Strong, A. W., Moskalenko, I. V., & Ptuskin, V. S. 2007, Annual Review of Nuclear and Particle Science, 57, 285
Strong, A. W., Moskalenko, I. V., & Reimer, O. 2000, ApJ, 537, 763
Strong, A. W., Moskalenko, I. V., & Reimer, O. 2004, ApJ, 613, 962
Su, M. & Finkbeiner, D. P. 2012, ApJ, 753, 61
Su, M., Slatyer, T. R., & Finkbeiner, D. P. 2010, ApJ, 724, 1044
Vladimirov, A. E., Digel, S. W., Johannesson, G., et al. 2011, Comput.Phys.Commun., 182, 1156
Wolleben, M. 2007, ApJ, 664, 349
Yang, R., Aharonian, F., & Evoli, C. 2016, Phys. Rev. D, 93, 123007
Yusef-Zadeh, F., Hewitt, J. W., Arendt, R. G., et al. 2009, ApJ, 702, 178

Appendix A: Modeling and systematic uncertainties

In this appendix we study the dependence of the spectrum of gamma-ray emission at the base of the FB on the selection of the low-energy range in the definition of the diffuse foreground model and on the choice of the class of the events (UltraCleanVeto vs. Source). We use the rectangles model of the FB in Section 3.3 as our baseline. In this model, the foreground emission template consists of Source data integrated over the energy interval $0.3 - 1.0\,\mathrm{GeV}$. To probe the dependence on the choice of the low-energy range in the model, we pick three non-overlapping energy ranges $0.3 - 0.5\,\mathrm{GeV}$, $0.5 - 1.0\,\mathrm{GeV}$, and $1.0 - 2.2\,\mathrm{GeV}$ and use the same analysis as for the baseline model. We also compare with the spectra obtained using UltraCleanVeto data both in the definition of the model at low energies and in the analysis at high energies. The residual spectra resulting from the different energy ranges and data classes are shown in Figure A.1. The agreement among the models is reasonably good at $E > 10$ GeV, especially for negative longitudes.

As one can see from Figure A.1, the highest-energy spectral point for negative longitudes may have an upward statistical fluctuation, which can influence the conclusions about the lower limit in the cutoff values. In order to test the dependence on the highest-energy spectral point, we exclude the energy bin 680 GeV − 1 TeV and repeat the derivation of the best-fit parameters in the rectangles model of the FBs. The results are presented in Table A.1. Without the last data point, the four areas with "infinite" cutoff energy have now a finite cutoff, but with a significance $2\Delta \log L < 1$, i.e., the models are still consistent with a simple power law. The 95% confidence lower limit on the cutoff value is also smaller for the dataset without the last point, but in this case we are using the data up to 680 GeV rather than 1 TeV.

Appendix B: Gamma distribution as a likelihood for smoothed data

In this appendix we show that smoothing the data and using gamma distribution instead of the Poisson distribution is a reasonable procedure (at least in the case when the scale of variations in the diffuse emission is larger than the smoothing radius). We split the log likelihood into a sum over areas with size approximately equal to the smoothing scale and neglect the correlation between the different areas after smoothing the data. Suppose that one of these areas has n pixels with random counts k_i drawn from a Poisson distribution with mean λ_0 (here we assume that the underlying diffuse flux is approximately constant within the smoothing radius). The likelihood function for parameter λ is

$$L(\lambda) = \prod_i \frac{\lambda^{k_i}}{k_i!} e^{-\lambda}. \tag{B.1}$$

The log likelihood is

$$\log L = \sum_{i=1}^{n} (-\lambda + k_i \log \lambda) + const. \tag{B.2}$$

The maximum likelihood value λ_* is determined from

$$0 = \frac{\partial \log L}{\partial \lambda} = -n + \frac{1}{\lambda} \sum_{i=1}^{n} k_i, \tag{B.3}$$

which gives $\lambda_* = \frac{1}{n} \sum_{i=1}^{n} k_i$. The uncertainty is

$$\frac{1}{\sigma^2} = - \left. \frac{\partial^2 \log L}{\partial \lambda^2} \right|_{\lambda=\lambda_*} = \frac{n}{\lambda_*}, \tag{B.4}$$

which gives $\sigma^2 = \lambda_*/n$.

If the smoothing radius is comparable to the size of the region, then we can approximate the values k_i with the average in the region $\tilde{k}_i = \bar{k} = \frac{1}{n} \sum_{i=1}^{n} k_i$ (note that $\tilde{k}_i$ are not integers). We take the gamma distribution for the likelihood function

$$\tilde{L} = \prod_i \frac{\lambda^{\tilde{k}_i}}{\Gamma(\tilde{k}_i + 1)} e^{-\lambda}. \tag{B.5}$$

The log likelihood is

$$\log \tilde{L} = \sum_{i=1}^{n} (-\lambda + \tilde{k}_i \log \lambda) + const. \tag{B.6}$$

The maximum likelihood solution is the same as in the Poisson case $\tilde{\lambda}_* = \bar{k} = \lambda_*$. The uncertainty is

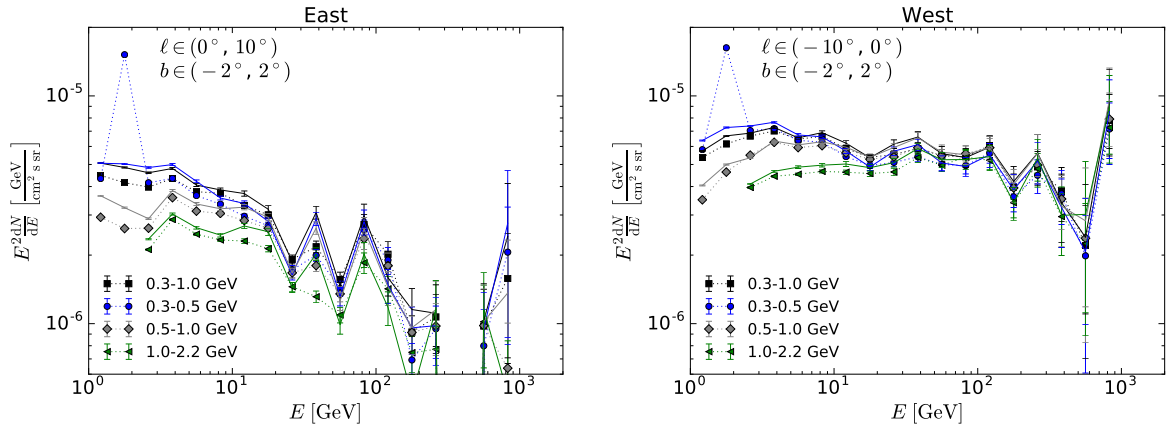


Fig. A.1: SED of the residual in the rectangles model using Source class (dotted lines with markers) and UltraCleanVeto class data (solid lines) in four different energy ranges used to determine the foreground diffuse emission template. The baseline model, presented in Section 3.3, has the low-energy range in the definition of the foreground model $0.3 - 1.0\,\text{GeV}$ (black squares).

Table A.1: Best-fit parameters of the rectangles model without the last energy bin: 680 GeV − 1 TeV. The definitions of the columns are the same as in Table 1.

Lat	Lon	N_0 $10^{-6}\,\text{GeV}^{-1}\text{cm}^{-2}\text{s}^{-1}\text{sr}^{-1}$	n	E_{cut} GeV	$2\Delta \log \mathcal{L}$	$E_{\text{cut},95\%}$ GeV	$E^{\text{min}}_{\text{cut},95\%}$ GeV
$(2^\circ, 6^\circ)$	$(0^\circ, 10^\circ)$	1.5 ± 0.4	1.9 ± 0.2	45 ± 22	6.8	25	25
	$(-10^\circ, 0^\circ)$	3.0 ± 0.4	2.2 ± 0.07	720 ± 1100	0.45	210	210
$(-2^\circ, 2^\circ)$	$(0^\circ, 10^\circ)$	6.1 ± 1.0	2.3 ± 0.08	660 ± 1000	0.42	180	2.0
	$(-10^\circ, 0^\circ)$	7.5 ± 0.8	2.1 ± 0.04	1400 ± 1500	0.76	490	460
$(-6^\circ, -2^\circ)$	$(0^\circ, 10^\circ)$	2.5 ± 0.3	2.1 ± 0.07	260 ± 160	3.4	130	2.3
	$(-10^\circ, 0^\circ)$	3.9 ± 0.4	2.1 ± 0.05	790 ± 820	0.96	290	290

also the same as in the Poisson case:

$$\frac{1}{\tilde{\sigma}^2} = -\left.\frac{\partial^2 \log \tilde{L}}{\partial \lambda^2}\right|_{\lambda=\tilde{\lambda}_*} = \frac{n}{\tilde{\lambda}_*} = \frac{1}{\sigma^2}. \tag{B.7}$$

Thus, smoothing the data and using the gamma distribution (in this case) gives the same result as using the original Poisson distribution, which shows that the procedure is well defined from the statistical point of view and it gives reasonable results.

Appendix C: Modeling uncertainty of ISRF near the GC

In this appendix we discuss the uncertainty of the IC model of the gamma-ray emission at the base of the FBs related to modeling of the ISRF near the GC. In order to estimate this uncertainty, we compare the ISRF model of Porter et al. (2008) (available with the distribution of GALPROP v54.1), the ISRF model of Popescu et al. (2017), and two ISRF models of Porter et al. (2017): R12, based on Robitaille et al. (2012), and F98, based on Freudenreich (1998). In Figure C.1 we show the corresponding densities of ISRFs averaged over the cylinder with the radius $R = 1.5$ kpc and the height $z = \pm 0.3$ kpc around the GC, which approximately corresponds to the latitude stripe $|b| < 2^\circ$ and $|\ell| < 10^\circ$. We notice that there can be up to a factor of 2 differences in the ISRF energy density at the peak of the SL emission (around 1 μm) and an order of magnitude differences in the IR wavelengths (around 100 μm), which can affect the inferred populations of CR electrons producing the IC gamma rays (see also Porter et al. 2017; Niederwanger et al. 2019).

In Figure C.2 we show the IC models of the gamma-ray emission at the base of the FBs in the rectangle $b \in (-2^\circ, 2^\circ)$, $\ell \in (-10^\circ, 0^\circ)$ for the different ISRF models near the GC. We separate the SL, IR, and CMB contributions. The SL and IR ISRFs are separated by splitting the radiation field energy densities at 0.1 eV (≈ 12 μm). We model the CR electrons spectra by a power-law function with an exponential cutoff. We fix the cutoff at 1 PeV and fit the normalization and the spectral index by fitting the IC model to the *Fermi*-LAT spectral points. The corresponding parameters are presented in Ta-

Table C.1: Spectra of CR electrons near the GC relative to the reference model based on the ISRF calculation of Porter et al. (2008) used in GALPROP v54.1.

ISRF model	Relative normalization at 1 GeV	Index
Porter et al. (2008)	1	2.71
Porter et al. (2017) R12	0.59	2.61
Porter et al. (2017) F98	1.16	2.71
Popescu et al. (2017)	1.64	2.79

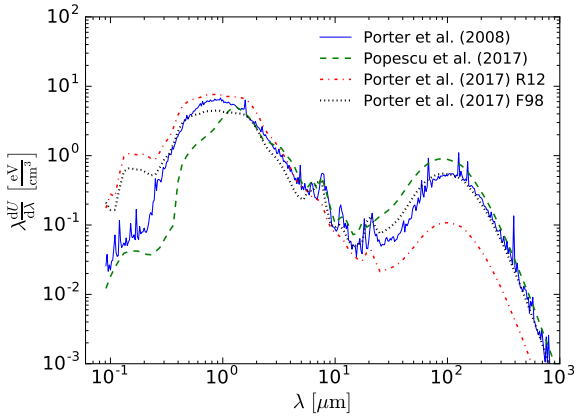


Fig. C.1: Comparison of ISRF SEDs at the GC (see text for more details).

ble C.1. We use the Porter et al. (2008) ISRF as the reference model and show the normalizations of the CRe spectra relative to the reference model (the normalizations are determined at 1 GeV). The overall spread in the normalizations is about a factor of 3, while the overall variation of the index of the CRe spectra is less than about 0.2.

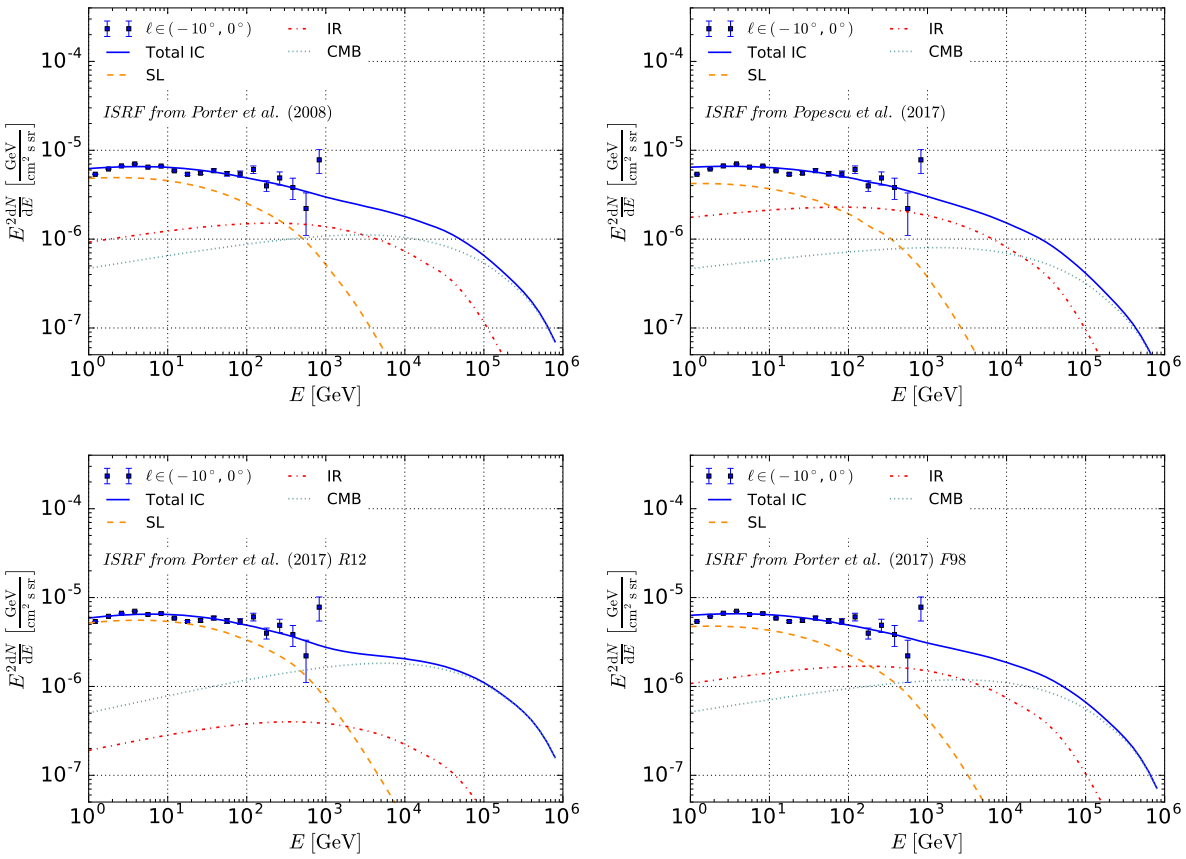


Fig. C.2: Contribution of different components of ISRFs to the IC model of the gamma-ray emission. The data points correspond to the emission at the base of the FBs in the rectangle $b \in (-2^\circ, 2^\circ)$, $\ell \in (-10^\circ, 0^\circ)$ (middle panel in Figure 11). The spectrum of CR electrons is modeled as a power-law function with an exponential cutoff at 1 PeV. We separate the SL and the IR contributions to the ISRF by formally splitting the ISRF at 0.1 eV.